Cell

The RIP1/RIP3 Necrosome Forms a Functional Amyloid Signaling Complex Required for Programmed Necrosis

Jixi Li,[1,6] Thomas McQuade,[2] Ansgar B. Siemer,[3,7] Johanna Napetschnig,[1] Kenta Moriwaki,[2] Yu-Shan Hsiao,[4] Ermelinda Damko,[1] David Moquin,[2] Thomas Walz,[4,5] Ann McDermott,[3] Francis Ka-Ming Chan,[2] and Hao Wu[1,6,*]
[1]Department of Biochemistry, Weill Cornell Medical College, New York, NY 10065, USA
[2]Department of Pathology, Program in Immunology and Virology, The University of Massachusetts Medical School, Worcester, MA 01655, USA
[3]Department of Chemistry, Columbia University, 3000 Broadway, New York, NY 10027, USA
[4]Department of Cell Biology
[5]Howard Hughes Medical Institute
Harvard Medical School, Boston, MA 02115, USA
[6]Present address: Program in Cellular and Molecular Medicine, Immune Disease Institute, Children's Hospital Boston and Department of Biological Chemistry and Molecular Pharmacology, Harvard Medical School, Boston, MA 02115, USA
[7]Present address: Department of Biochemistry and Molecular Biology, Zilkha Neurogenetic Institute, Keck School of Medicine of the University of Southern California, Los Angeles, CA 90033, USA
*Correspondence: hao.wu@childrens.harvard.edu
http://dx.doi.org/10.1016/j.cell.2012.06.019

SUMMARY

RIP1 and RIP3 kinases are central players in TNF-induced programmed necrosis. Here, we report that the RIP homotypic interaction motifs (RHIMs) of RIP1 and RIP3 mediate the assembly of heterodimeric filamentous structures. The fibrils exhibit classical characteristics of β-amyloids, as shown by Thioflavin T (ThT) and Congo red (CR) binding, circular dichroism, infrared spectroscopy, X-ray diffraction, and solid-state NMR. Structured amyloid cores are mapped in RIP1 and RIP3 that are flanked by regions of mobility. The endogenous RIP1/RIP3 complex isolated from necrotic cells binds ThT, is ultrastable, and has a fibrillar core structure, whereas necrosis is partially inhibited by ThT, CR, and another amyloid dye, HBX. Mutations in the RHIMs of RIP1 and RIP3 that are defective in the interaction compromise cluster formation, kinase activation, and programmed necrosis in vivo. The current study provides insight into the structural changes that occur when RIP kinases are triggered to execute different signaling outcomes and expands the realm of amyloids to complex formation and signaling.

INTRODUCTION

Recent studies have implicated the intracellular signaling kinase RIP1 as a key switch of cell fate regulation. Depending on the cellular context, RIP1 controls whether the pleiotropic cytokine TNF induces NF-κB activation, apoptosis, or programmed necrosis (Moquin and Chan, 2010). The E3 ligases cIAP1/2 and LUBAC ubiquitinate RIP1 in the TNFR1 signaling complex (Walczak, 2011). Polyubiquitinated RIP1 then engages downstream adaptors such as NEMO to activate IKK to promote NF-κB transcriptional activity, leading to cell survival, proliferation, and differentiation (Walczak, 2011). When RIP1 ubiquitination is blocked by removal of the E3 ligases cIAP1 and cIAP2 through genetic ablation, RNA interference (RNAi) knockdown, or inhibitor of apoptosis (IAP) antagonists, RIP1 forms a secondary complex in the cytosol with Fas-associated death domain (FADD) and caspase-8—termed the Ripoptosome—to initiate apoptotic cell death (Feoktistova et al., 2011; Tenev et al., 2011; Wang et al., 2008). Active caspase-8 within the Ripoptosome cleaves and inactivates RIP1 (Chan et al., 2003; Lin et al., 1999) and RIP3 (Feng et al., 2007). When caspases are inhibited by pharmacological inhibitors or under certain physiological conditions such as viral infections, RIP1 and RIP3 form the necrosome to initiate a third pathway known as programmed necrosis or necroptosis (Cho et al., 2009; He et al., 2009; Zhang et al., 2009).

The understanding of programmed necrosis is still unfolding. Whereas it was originally thought to be associated with nonspecific cellular damages, genetic experiments in mice clearly show that caspase-8-mediated cleavage and inactivation of RIP1 and RIP3 is critical for preventing extensive necrosis during embryonic development in order to ensure proper clonal expansion of lymphocytes and to prevent extensive necrosis and inflammation in skin and intestinal epithelium (Kaiser et al., 2011; Oberst et al., 2011; Welz et al., 2011; Zhang et al., 2011). In addition to caspase inhibition, assembly of the RIP1/RIP3 necrosome also requires intact RIP1 and RIP3 kinase activity (Cho et al., 2009). Recent studies identified MLKL, a kinase-like protein, as a substrate of the RIP3 kinase (Sun et al., 2012; Zhao et al., 2012).

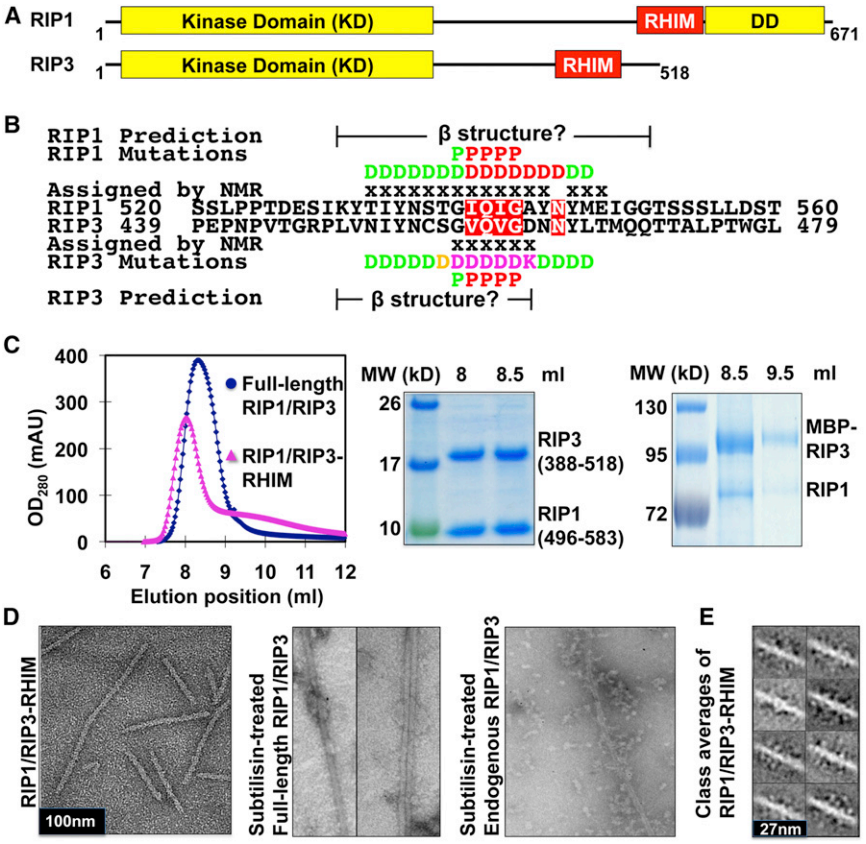

Figure 1. RIP1 and RIP3 Form a Filamentous Complex In Vitro and in Cells

(A) Domain organization of human RIP1 and RIP3.

(B) Sequence alignment of RIP1 and RIP3 around the core RHIMs. Residues in RIP1 and RIP3 that are conserved across different species (Figure S1) are highlighted in red. Regions predicted to be in β sheet conformations are shown. Residues assigned by solid-state NMR are marked with "x." Summary of mutagenesis results are displayed, with red indicating most defective mutants showing complete or partial dissociation between RIP1 and RIP3, magenta indicating defective mutants showing smaller complexes, orange indicating partially defective mutants with size of the complex between that of WT and defective mutants, and green indicating nondefective mutants.

(C) Coexpressed full-length and truncated RIP1/RIP3 complexes. Left, superimposed gel filtration profiles. Right, SDS-PAGE of the fractions.

(D) EM images of the RIP1/RIP3 complex.

(E) Representative class averages of the RIP1/RIP3-RHIM fibrils.

See also Figure S1.

The structural basis for the association between RIP1 and RIP3 within the necrosome is poorly understood. Both RIP1 and RIP3 contain Ser/Thr kinase domains (KDs) at their N-termini, and RIP1 also has a death domain (DD) at its C terminus for recruitment to the TNF receptor signaling complex (Stanger et al., 1995; Sun et al., 1999; Yu et al., 1999) and for formation of the Ripoptosome (Feoktistova et al., 2011; Tenev et al., 2011; Wang et al., 2008) (Figure 1A). Unique segments of homologous sequences in RIP1 and RIP3 (RIP homotypic interaction motifs, RHIMs) (Figures 1A and 1B) were shown to mediate their interaction (Sun et al., 2002), which is crucial for the induction of programmed necrosis (Cho et al., 2009). The RHIM is found in a growing number of signaling adaptors with crucial functions in cell death and innate immunity (Moquin and Chan, 2010). For instance, macrophage necrosis induced through TLR-3/4 requires RHIM-mediated interaction between the adaptor TRIF and RIP3 (He et al., 2011). Similarly, RHIM-mediated interaction between the intracellular DNA sensor DAI and RIP3 causes necrosis of cells infected with murine cytomegalovirus (Upton et al., 2012).

Here, we show that RIP1 and RIP3 form an amyloid structure through their RHIMs and that this heterodimeric amyloid structure is a functional signaling complex that mediates programmed necrosis. Our results not only provide insights into the mechanism of RIP1 and RIP3 kinase activation but also further expand the realm of amyloid structures to normal physiological functions beyond those associated with human diseases (Eisenberg and Jucker, 2012).

RESULTS

The RIP1/RIP3 Complex Forms Filamentous Structures In Vitro and in Cells

The exact boundaries of RHIMs are unclear, but the sequence conservation is centered around the I(V)QI(V)G motif (Figure 1B and Figure S1A available online). We coexpressed RHIMs of RIP1 (residues 496–583) and His-tagged RIP3 (residues 388–518) (RIP1/3-RHIM) using regions that were previously shown to be sufficient for complex formation (Sun et al., 2002). The RIP1/3-RHIM complex copurified from Ni-affinity chromatography eluted around the void position of a Superdex 200 10/300 GL gel filtration column, which is much larger than the expected molecular mass of a heterodimer (Sun et al., 2002) (Figure 1C). We then coexpressed full-length RIP1 and RIP3 (RIP1/3-FL) in insect cells, which similarly coeluted around the void position of the gel filtration column (Figure 1C).

We investigated why RIP1/3-RHIM and RIP1/3-FL could form such large complexes. Secondary structure predictions suggested that the region between the KD and the DD in RIP1 (~residues 300–560) and the region C-terminal to the KD in RIP3 (~residues 300-end) are mostly unstructured random coils (Rost et al., 2004). The only exceptions are short segments of sequences around the I(V)QI(V)G motif, which show propensities for β strands (Figure 1B). Because amyloids are fibrous protein aggregates composed of cross-β cores, we asked whether RHIMs mediate assembly of amyloid-like fibrils.

We used electron microscopy (EM) to visualize the structures of the RIP1/RIP3 complexes. Consistent with our hypothesis, EM of negatively stained RIP1/3-RHIM revealed filamentous structures (Figure 1D). The fibrils exhibit a similar width of ~11–12 nm but vary in length. Class averages show substantial

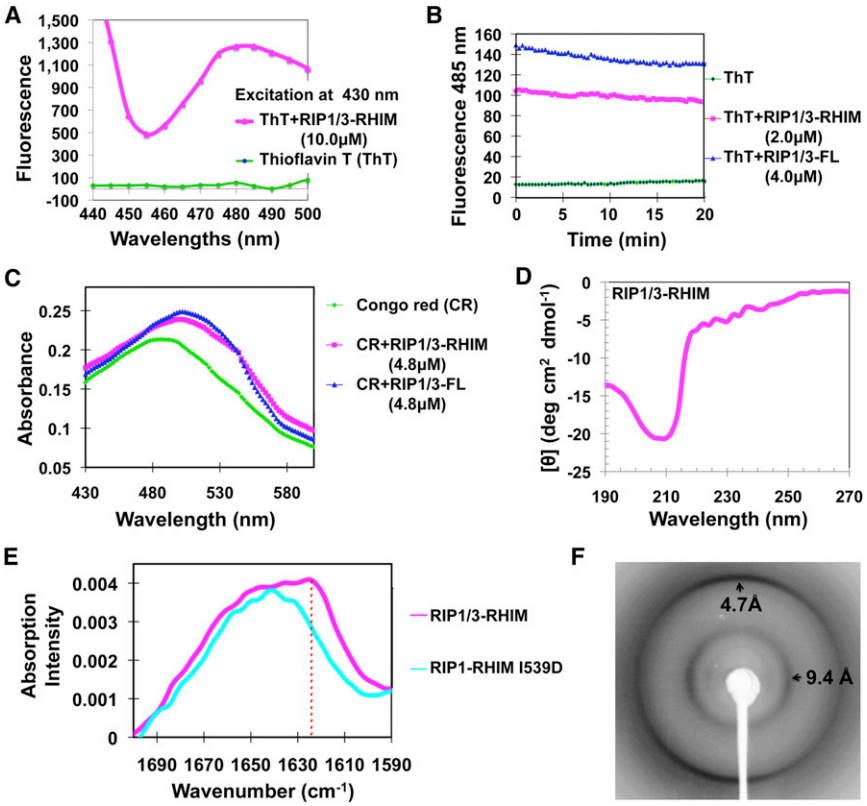

Figure 2. The RIP1/RIP3 Complex Is Amyloidal

(A) Fluorescence emission spectra of ThT in the absence (green) and presence (magenta) of the RIP1/RIP3-RHIM complex.

(B) Both the RIP1/RIP3-RHIM and the full-length RIP1/RIP3 complex bind ThT.

(C) Absorption spectra of CR in the absence (green) and presence of either RIP1/RIP3-RHIM (magenta) or full-length RIP1/RIP3 complex (blue).

(D) Circular dichroism spectrum of the RIP1/RIP3-RHIM complex.

(E) Superimposed Fourier transform infrared spectra of RIP/RIP3-RHIM (magenta) and the I539D mutant of RIP1 (cyan). Only the WT RIP1/RIP3 complexes, not the RHIM mutant, showed the amide I′ maxima at 1,623 cm^{-1} (dashed vertical red line), which is characteristic of β-amyloid.

(F) An X-ray diffraction image of partially aligned RIP1/RIP3 fibrils. The arrows indicate equatorial and meridional reflections at 9.4 Å and 4.7 Å resolutions, respectively.

See also Figure S2.

structural variability, but closer inspection suggests that the core of the complex, ~8 nm, may be ordered and that the variability may be mostly due to flexible extensions (Figure 1E). EM of negatively stained RIP1/3-FL showed mostly aggregates. We reasoned that the KDs and DD in full-length RIP1 and RIP3 might mediate additional interactions and mask the central amyloidal fibril architecture. Upon limited proteolysis to remove the flanking domains by subtilisin, the same enzyme used in the nuclear magnetic resonance (NMR) sample preparation (see section "Amyloid Core of the RIP1/RIP3 Complex"), clear fibril structures were revealed for RIP1/3-FL, similar to RIP1/3-RHIM (Figure 1D). When endogenous RIP1/RIP3 complex from HT-29 cells immunoprecipitated with anti-RIP1 antibody was treated with subtilisin and negatively stained, it showed mostly short and sometimes long filamentous structures under EM only upon necrosis induction with TNF, zVAD-fmk, and the IAP antagonist LBW242, but not before induction (Figures 1D and S1B).

The RIP1/RIP3 Complex Exhibits Classical Characteristics of Amyloid Fibrils

Amyloids are classically characterized using aromatic, cross-β binding dyes such as Thioflavin T (ThT) (LeVine, 1999) and Congo red (CR) (Klunk et al., 1989). To determine whether the RIP1/RIP3 fibrils are indeed amyloidal, we first characterized purified recombinant RIP1/RIP3 complexes in vitro. We added ThT to either RIP1/3-RHIM or RIP1/3-FL and measured its fluorescence after excitation at 430 nm. In comparison to ThT alone, RIP1/3-RHIM and RIP1/3-FL caused ThT to display an emission peak at ~485 nm with concomitant increase in fluorescence intensity (Figures 2A, 2B, and S2A). Similarly, CR showed a characteristic red shift from an absorption maximum of ~470 nm to ~540 nm upon addition of either RIP1/3-RHIM or RIP1/3-FL (Figures 2C and S2B) (Klunk et al., 1989). Therefore, both the ThT- and the CR-binding assays confirmed that the RIP1/RIP3 complex is amyloidal.

We then used circular dichroism (CD) to estimate the secondary structure content of RIP1/3-RHIM, which revealed a prominent negative peak at ~210 nm (Figure 2D). Analysis of the spectrum with DICHROWEB (Whitmore and Wallace, 2004) indicated that the sample is a mixture of β sheet and random coil structures. Fourier transform infrared spectroscopy (FTIR) has been well established to distinguish cross-β amyloid fibrils from native β sheet proteins in that the former shows amide I′ maxima between 1,610 cm^{-1} and 1,630 cm^{-1} in wavenumbers, which is smaller than native β sheet proteins (Zandomeneghi et al., 2004). This difference has been attributed to smaller β sheet twist angles and larger numbers of β strands in amyloidal aggregates (Zandomeneghi et al., 2004). Indeed, RIP1/3-RHIM showed a prominent amide I′ absorbance maximum at 1,623 cm^{-1} (Figure 2E), which is consistent with the amyloidal nature of the complex. The RIP1-RHIM mutant I539D, which is no longer amyloidal (see section "Mutations of RIP1 and RIP3 Weaken Filament Formation"), did not exhibit this characteristic absorption.

Amyloids are characterized by cross-β quaternary structures in which the β sheets are parallel to the fiber axis, and the extended β strands lie approximately perpendicular to the axis. This arrangement produces characteristic diffraction patterns (Sunde et al., 1997). We partially aligned the RIP1/3-RHIM complex and obtained its diffraction pattern by using

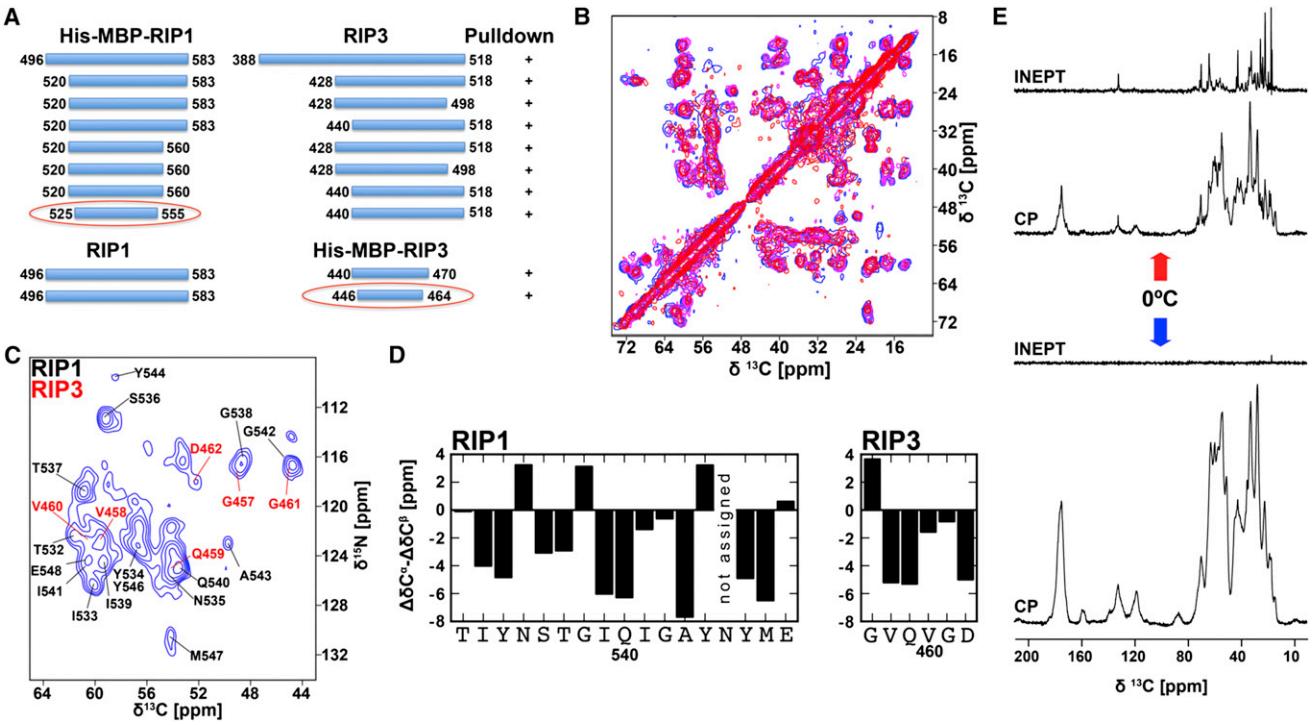

Figure 3. The Amyloid Core of the RIP1/RIP3 Complex

(A) Mapping the interaction between RIP1 and RIP3 by using coexpression and His-tag pull-down. The shortest constructs that retained interaction are circled in red.

(B) Overlay of 2D DARR ^{13}C-^{13}C solid-state NMR spectra of the RIP1 (residues 496–583)/RIP3 (residues 388–518) complex (blue), its subtilisin-digested counterpart (magenta), and the RIP1 (residues 496–583)/RIP3 (residues 446–518) complex (red).

(C) 2D ^{15}N-^{13}C NCA solid-state NMR spectrum of subtilisin-digested RIP1/RIP3 complex. Site-specific assignments are indicated for RIP1 (black) and RIP3 (red).

(D) Plot of the difference in secondary chemical shift between Cα and Cβ, indicative of secondary structures (only ΔδCα for Gly).

(E) ^{13}C 1D NMR spectra of the RIP1 (residues 496–583)/RIP3 (residues 388–518) complex. At above 0°C (top), the line width is generally narrower, and the INEPT pulse sequence, which is sensitive to relatively dynamic domains of the sample, gives an intense spectrum. At below 0°C (bottom), most of the dynamics are arrested, leading to no signal in the INEPT and an intense and broad cross-polarization (CP) spectrum, which is sensitive to the static domains of the sample. See also Figure S3.

Cu radiation (Figure 2F). Orthogonal diffractions at 4.7 Å and 9.4 Å resolutions were observed, corresponding to the inter-β strand spacing along the meridional axis (parallel to the fibril axis) and the inter-β sheet stacking distance along the equatorial direction (perpendicular to the fibril axis), respectively. These data established unequivocally the cross-β amyloid core of the RIP1/RIP3 complex.

The Amyloid Core of the RIP1/RIP3 Complex

Secondary structure prediction suggests that the amyloid core sequences of RIP1 and RIP3 are much shorter than either the full-length or the truncated coexpression construct we used for obtaining the RIP1/RIP3 complex. To further map this interaction, we generated a series of coexpression constructs tagging either RIP1 or RIP3 with a His-MBP tag. His-tag pull-down experiments of the coexpression constructs showed that the interaction was retained, even when RIP1 was only 31 residues (525–555) and RIP3 was only 19 residues (446–464) in length (Figures 3A, S3A, and S3B).

To further elucidate the core size and the secondary structure of the RIP1/RIP3 complex, we used solid-state NMR. Because sample conditions may influence amyloid structures, we collected 2D DARR ^{13}C-^{13}C correlation spectra at ~10°C from three different coexpressed constructs, the RIP1 (residues 496–583)/RIP3 (residues 388–518) complex, its subtilisin-digested counterpart, and the RIP1 (residues 496–583)/RIP3 (residues 446–518) complex. The overlay of these spectra showed very strong correspondence (Figure 3B), indicating that the size and the structure of the RIP1/RIP3 amyloid core are robust with respect to construct lengths and details of the preparation.

To obtain sequence-specific secondary structure information, we recorded high-resolution ^{13}C-^{13}C dipolar recoupling enhanced by amplitude modulation (DREAM) and dipolar-assisted rotational resonance (DARR) spectra; ^{15}N-^{13}C NCO, NCA, NcaCB, and NcoCX 2D spectra; and NCACX and NCACB 3D spectra on the subtilisin-digested complex at ~10°C (Figures S3C, S3D). Using the mapped amyloid core sequences (Figures 1B and 3A) as targets, the majority of the peaks in the NCA spectrum were assigned, with 16 residues of RIP1 (T532–Y544 and Y546–E548) and 6 consecutive residues of RIP3 (G457–D462) (Figures 3C and 3D). Some of the residues were assigned with high confidence due to the nondegenerate ^{15}N and ^{13}C peaks

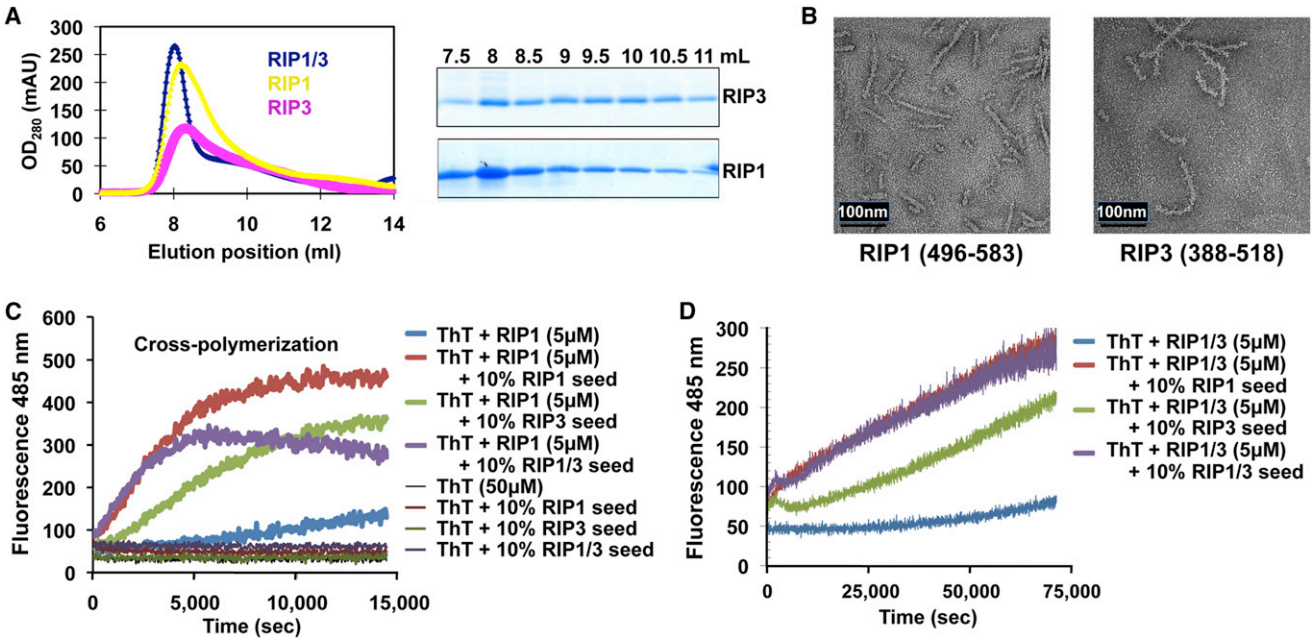

Figure 4. Cross-Polymerization and Mutagenesis of the RIP1/RIP3 Interaction

(A) Left, superimposed gel filtration profiles of the RHIM fragments of RIP1 (residues 496–583), RIP3 (residues 388–518), and the RIP1/RIP3 complex. Right, SDS-PAGE of gel filtration fractions of RIP1 and RIP3.

(B) EM images of RIP1 and RIP3.

(C and D) Cross-seeding in the polymerization of denatured RIP1 and the denatured RIP1/RIP3 complex by using ThT binding assays, respectively.

See also Figure S4.

in the three-dimensional (3D) spectra with additional support from C^{α}-C^{α}-1 cross-peaks in the two-dimensional (2D) DARR spectrum. All assignments are consistent with the RIP1/RIP3 core sequences. Negative and positive values of the difference in secondary chemical shifts between C^{α} and C^{β} (i.e., $\Delta\delta C^{\alpha}$-$\Delta\delta C^{\beta}$ or δC^{α} for Gly) are indicative of β sheet and α-helical conformations, respectively. Most of the residues in the amyloid core are compatible with β sheet conformations, and the 4 central RHIM residues show consecutive negative shift differences (Figures 3D and S3E).

The spectra recorded with cross-polarization (CP)-based solid-state NMR above 0°C can be explained by ~37 resolved residues. Most of the residues outside the β-amyloid core were unobserved and either too dynamic or disordered to be visible in these spectra. Fast molecular dynamics can lead to partial or complete averaging of dipolar spin couplings that are essential for CP to work. When ^{1}H-^{13}C insensitive nuclei enhanced by polarization transfer (INEPT)—a sequence that only works when dipolar couplings are absent—was utilized, we observed intense and narrow spectra (Figure 3E). This indicated that there are very dynamic domains outside the amyloid core. This observation is consistent with the small core size observed from class averages of EM images (Figure 1E). At lower temperatures, these dynamics slowed down so that more domains in the sample could be detected with CP, but not with INEPT (Figure 3E).

Cross-Polymerization of the RIP1/RIP3 Complex

The sequence conservation at the core of the RHIMs of RIP1 and RIP3 prompted us to ask whether RIP1 or RIP3 alone could also form amyloid fibrils. Expression of His-Sumo-RIP1 (residues 496–583) or His-Sumo-RIP3 (residues 388–518) alone, followed by cleavage of the respective His-Sumo tag, showed that RIP1-RHIM or RIP3-RHIM eluted around the void position from a gel filtration column (Figure 4A). The RIP1 and RIP3 CD spectra showed similar secondary structures as the RIP1/RIP3 complex, and ThT fluorescence and CR absorption confirmed their amyloidal structures (Figure S4). EM of negatively stained RIP1 and RIP3 samples revealed that the homocomplexes are able to form fibrils by themselves as well (Figure 4B). However, these fibrils appeared to be less regular and shorter than those of the RIP1/RIP3 heterocomplex (Figure 1D).

Because RIP1 and RIP3 can each form fibrils on their own, we wondered whether the observed fibrils are similar to that of the RIP1/RIP3 complex. To address this question, we performed cross-fibril polymerization experiments to see whether the amyloids of RIP1, RIP3, or the RIP1/RIP3 complex can enhance the polymerization of each other. Because the purified recombinant proteins are already fibrillar, we needed to first denature the proteins. Consistent with the recognized high stability of amyloid structures (Balbirnie et al., 2001), we had to use harsh conditions: 8 M urea for RIP1 and 150 mM NaOH for the RIP1/RIP3 complex. When RIP1 was first denatured and then diluted 100-fold into the native ThT binding buffer to allow refolding, it showed minimal enhancement of ThT fluorescence as a function of time. When the same denatured RIP1 was subsequently diluted to allow renaturation in the presence of 10% native RIP1, RIP3, or the RIP1/RIP3 complex as polymerization seeds, ThT fluorescence increased much more quickly (Figure 4C).

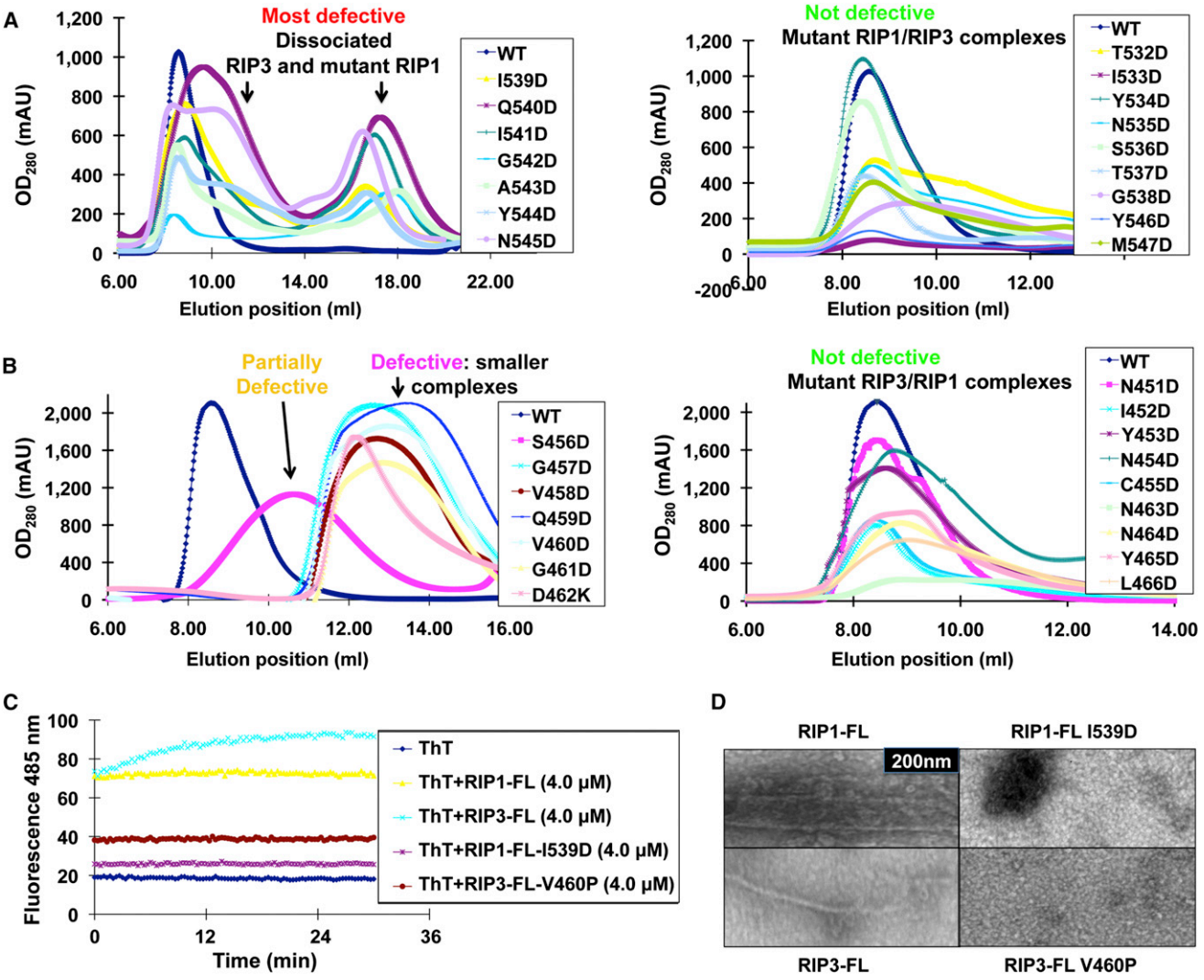

Figure 5. Mutagenesis of RIP1 and RIP3

(A) Superimposed gel filtration profiles of complexes of mutant RIP1 and WT RIP3. Left, RIP1 mutants that dissociated from RIP3; right, RIP1 mutants that did not dissociate from RIP3 and migrated near the void position.

(B) Superimposed gel filtration profiles of complexes of mutant RIP3 and WT RIP1. Left, complexes of mutant RIP3 and WT RIP1 that migrated later than the void position; right, complexes of mutant RIP3 and WT RIP1 that migrated near the void position.

(C) ThT fluorescence of WT and mutant full-length RIP1 and RIP3.

(D) EM images of negatively stained WT and mutant full-length RIP1 and RIP3.

See also Figure S5.

Similarly, denatured RIP1/RIP3 complex can be induced to polymerize much more efficiently in the presence of 10% native seeds of RIP1, RIP3, or the RIP1/RIP3 complex (Figure 4D). These experiments suggest that the fibrils of RIP1 and RIP3, as well as the RIP1/RIP3 complex, share a similar structural architecture.

Mutations of RIP1 and RIP3 Weaken Filament Formation

To elucidate the key determinants in RIP1/RIP3 interaction, we generated point mutations on residues spanning the core RHIMs of RIP1 and RIP3. Residues 533–548 of RIP1 and residues 451–466 of RIP3 were mutated to Asp for possible maximal disruptive effects, except that D461 of RIP3 was mutated to Lys (Figure 1B). The RHIM consensus sequences were also mutated to Pro (Figure S5). For RIP1 mutants, we used a coexpression construct of His-RIP1 (residues 496–583) and RIP3 (residues 388–518). For RIP3 mutants, a coexpression construct containing an untagged wild-type (WT) RIP1 and a His-tagged RIP3 was used.

All mutant His-RIP1 proteins could pull down coexpressed WT RIP3 with Ni-affinity beads. However, when the copurified samples were subjected to gel filtration chromatography, clear differences appeared (Figures 1B and 5A). Whereas RIP1 mutants flanking the core RHIM did not show any defects in

RIP3 interaction or fibril formation, RIP1 mutants near the center of the RHIM (I539D, I539P, Q540D, Q540P, I541D, I541P, G542D, G542P, A543D, Y544D, and N545D) were the most defective (Figures 5A, S5A, and S5B). These RIP1 mutants dissociated from RIP3, as observed by the appearance of an additional RIP1 mutant peak at ~17 ml.

Similarly, all His-RIP3 point mutants could pull down coexpressed WT RIP1 with Ni-affinity beads. When these complexes were subjected to gel filtration chromatography, a range of effects occurred, including dissociation on gel filtration chromatography and a change in elution positions (Figures 1B, 5B, S5C, and S5D). Asp mutants on central RHIM residues of RIP3 "457-GVQVGD-462" eluted at around 12–14 ml in comparison with the void position of around 8 ml for the WT RIP1/RIP3 complex. S456D was also partially defective, as it eluted around 11 ml. The changes in the elution positions suggest that the mutant complexes have lower apparent molecular masses than the WT complex and exhibit weakened interaction between RIP1 and RIP3. A double mutant of the core RHIM of RIP3 (V458E and V460E) induced dissociation from WT RIP1 on gel filtration chromatography (Figure S5C). Pro mutants on central RHIM residues of RIP3 "458-VQVG-461" resulted in partial dissociation with coexpressed WT RIP1, and V460P and G461P were the most defective. In contrast, mutations on more peripheral residues "451-NIYNC-455" and "463-NNYL-466" migrated in a manner similar to the WT complex.

Similar to the results for the RHIM constructs of RIP1 and RIP3, mutations on full-length RIP1 and RIP3 also weakened or disrupted filament formation. ThT staining of insect cell-expressed recombinant RIP1-FL mutant I539D and RIP3-FL mutant V460P showed that both proteins exhibited close to background levels of ThT fluorescence in comparison to the WT proteins (Figure 5C). Upon subtilisin digestion, EM of WT RIP1-FL and RIP3-FL showed filamentous structures, though they were apparently less regular than the RIP1/RIP3 complex (Figures 5D and 1D). In contrast, the RIP1-FL mutant I539D and the RIP3-FL mutant V460P were mostly degraded by subtilisin and showed only residual aggregates (Figure 5D).

Amyloidal Nature and Ultrastability of the Endogenous RIP1/RIP3 Complex

To determine whether the fibrils of endogenous RIP1/RIP3 complex isolated from necrotic cells that we observed under EM (Figure 1D) are amyloidal in nature, we first used ThT binding. Because the amount of endogenous complexes isolated from cells was much lower than that obtained from recombinant proteins, we measured ThT fluorescence by using a more sensitive instrument. HT-29 cells stimulated with TNF, zVAD-fmk, and LBW242 underwent RIP1/RIP3-dependent programmed necrosis (He et al., 2009). The RIP1-containing complex isolated from necrotic cells, but not from control cells, exhibited increased ThT fluorescence in a concentration-dependent manner (Figure 6A).

Given that the recombinant RIP1/RIP3 complex is ultrastable and requires 150 mM NaOH to be denatured, we tested the stability of the endogenous complex isolated from necrotic cells. We lysed cells with buffers containing 4 M urea, 8 M urea, or 150 mM NaOH. Thirty minutes after lysis, we diluted the lysates 10-fold with regular nondenaturing lysis buffer. Immunoprecipitation with anti-RIP3 antibody showed that 4 M urea or 8 M urea did not disrupt the interaction between RIP3 and RIP1, whereas 150 mM NaOH did (Figure 6B). This result is consistent with the stability of the recombinant complex and with the recognized stability of amyloidal structures in general (Balbirnie et al., 2001). In contrast, the interaction between polyubiquitinated RIP1 and TNFR1, which is crucial for TNF-induced NF-κB activation, was completely abolished in all conditions, including 4 M urea (Figure 6C).

Classical β-amyloid-binding dyes often inhibit amyloid oligomerization (Sánchez et al., 2003). Pretreatment of HT-29 cells with CR (Figure 6D), ThT, or another β-amyloid-binding compound, 2-(2-hydroxyphenyl)-benzoxazole (HBX) (Alavez et al., 2011), inhibited necrosis in a dose-dependent manner (Figure 6E). The inhibition by ThT and HBX is specific for necrosis because they had no effect in apoptotic HT-29 cells (Figure S6A). Clustering of RIP1 and RIP3 into punctate-like structures is a distinct feature of necrosis (Figures S6B–S6D). This was confirmed by immunogold EM (Figure 6F). When HeLa cells, which do not express endogenous RIP3, were transfected with RIP3-mCherry and stimulated with TNF, zVAD-fmk, and LBW242 to induce necrosis, they showed complete overlap of ThT staining with RIP3-mCherry puncta (Figure 6G). By contrast, ThT signal was undetectable in untreated cells (Figure 6G). Collectively, these results definitively show that RIP1 and RIP3 form amyloidal complexes during induction of programmed necrosis.

RHIM Residues of RIP1 and RIP3 Are Crucial for Cluster Formation, Kinase Activation, and Programmed Necrosis

To determine the functional role of RHIMs in the assembly of the amyloidal RIP1/RIP3 complex in vivo, we introduced selected mutations within and flanking the RHIMs that were shown to cause disruption of filament formation and mutual interaction in vitro (Figure 1B). For RIP3, we stimulated HeLa cells transfected with WT and mutant RIP3-yellow fluorescent protein (YFP) with TNF, zVAD-fmk, and LBW242. As expected, WT RIP3-transfected cells underwent cell death, whereas the RHIM AAAA mutant was highly protected. Importantly, RIP3 mutants V458P, V460P, and G457D protected cells from TNF-induced necrosis, whereas the mutant N464D that did not show significant defects in vitro behaved most similar to the WT (Figure 7A). In addition, mutants V458P and V460P completely abolished puncta formation in response to necrosis stimulation, whereas G457D partially disrupted RIP3 clustering (Figure 7B). On the other hand, N464D still formed puncta (Figure 7B). Expression of RIP3-YFP in 293T cells showed that the mutations V458P and V460P severely compromised RIP3 kinase activation by using myelin basic protein (MBP) as the substrate (Figure S7A). To further validate the results from transient expression, we stably reconstituted RIP3$^{-/-}$ fibroblasts with WT and mutant RIP3. In agreement with results in 293T cells, WT RIP3 showed robust kinase activity upon induction of necrosis, whereas the V458P, V460P, and G457D mutants were dramatically impaired in kinase activation (Figure 7C). Notably, there is a close correlation between in vitro and in vivo experiments.

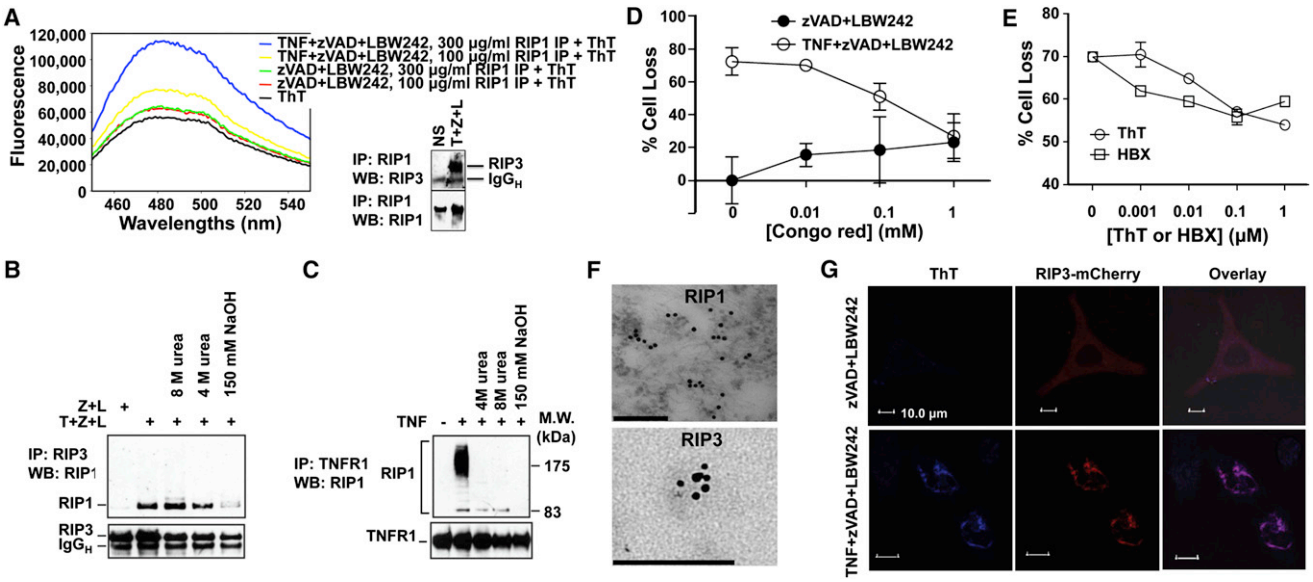

Figure 6. RIP1 and RIP3 Form Amyloidal Clusters In Vivo during Programmed Necrosis

(A) Endogenous RIP1-containing complexes from necrotic HT-29 cells bind ThT. The right panel shows the specific pull-down of RIP3 by RIP1 upon TNF, zVAD-fmk, and LBW242 stimulation (T+Z+L).

(B) RIP3 complexes isolated by immunoprecipitation from HT-29 cells treated with T+Z+L after lysis in regular lysis buffer or buffer containing the indicated amount of urea or NaOH.

(C) TNFR1 complexes isolated by immunoprecipitation from MEFs treated with TNF after lysis in regular lysis buffer or buffer containing the indicated amount of urea or NaOH.

(D and E) Amyloid-binding compounds inhibit TNF-induced necrosis in HT-29 cells. Results shown are averages of triplicates ±SEM.

(F) Clustering of RIP1 and RIP3 in necrotic MEFs shown by immunogold EM. Scale bars, 200 nm (RIP1) and 100 nm (RIP3).

(G) Costaining of ThT with RIP3 puncta in necrotic HeLa cells as visualized by confocal microscopy.

See also Figure S6.

For instance, V460P is the most defective in fibril formation and RIP1 interaction in vitro (Figure S5D; note the weakest RIP3 band in the fibril fraction) and is the most defective in cell death induction and kinase activation. Similarly, G457D is a less defective mutant in cell death induction and is also less impaired in kinase activation and cluster formation (Figures 7A–7C).

To assess RIP1 mutational phenotypes in vivo, we transfected RIP1$^{-/-}$ fibroblasts with WT and mutant RIP1-green fluorescent protein (GFP). Cell death upon necrosis induction was enumerated in the GFP^{+} population by using flow cytometry. Like the RHIM AAAA mutant, the RIP1 mutants I539P, I541P, and N545P were much weaker in mediating necrosis than WT RIP1 (Figure 7D), recapitulating the in vitro interaction data. Similar to evaluation of the kinase activity of RIP3 mutants, we expressed RIP1-GFP constructs in 293T cells. After immunoprecipitation with anti-GFP antibody, the immune complexes were subjected to in vitro kinase assay using MBP as the substrate. All three RIP1 mutants, I539P, I541P, and N545P, showed defective kinase activation (Figure 7E). We attempted to stably reconstitute RIP1$^{-/-}$ fibroblasts with WT and mutant RIP1; however, because RIP1 is generally expressed at much lower levels than RIP3, likely due to toxicity, we could not evaluate the kinase activities in these cells. Similar defects in clustering in mutations within the core RHIM residues were observed with truncated RIP1 (residues 496–583) and RIP3 (residues 388–518) lacking the KDs and DD (Figure S7B). Thus, these results define a critical role for RHIM-mediated amyloidal RIP1/RIP3 fibrils in the activation of RIP1/RIP3 kinase activity and the induction of programmed necrosis.

DISCUSSION

Amyloids are fibrous protein aggregates composed of cross-β structures and associated with many neurodegenerative (Chiti and Dobson, 2006) and infective prion diseases (Uptain and Lindquist, 2002). Amyloids can also perform normal cellular functions, such as host interaction, hazard protection, and memory storage (Chiti and Dobson, 2006). However, this aspect of the function of amyloids is less defined, especially in mammals. Here, we show that RIP1 and RIP3 form a functional, hetero-oligomeric amyloidal signaling complex that mediates programmed necrosis. The discovery of cross-β amyloid structures in protein complexation and signal transduction provides new insights into both the amyloid field and the signaling field.

How is the assembly of the RIP1/RIP3 necrosome regulated? It has been shown that both RIP1 and RIP3 kinase activities are required for complex formation and cell death (Cho et al., 2009). Consistent with a role for amyloid assembly in RIP1 and RIP3 kinase activation, hyperphosphorylated RIP1 and RIP3 are found predominantly in NP-40 insoluble fractions (Figures S6C and S6D). Interestingly, abnormal phosphorylation of tau and α-synuclein by multiple kinases is known to be involved in the

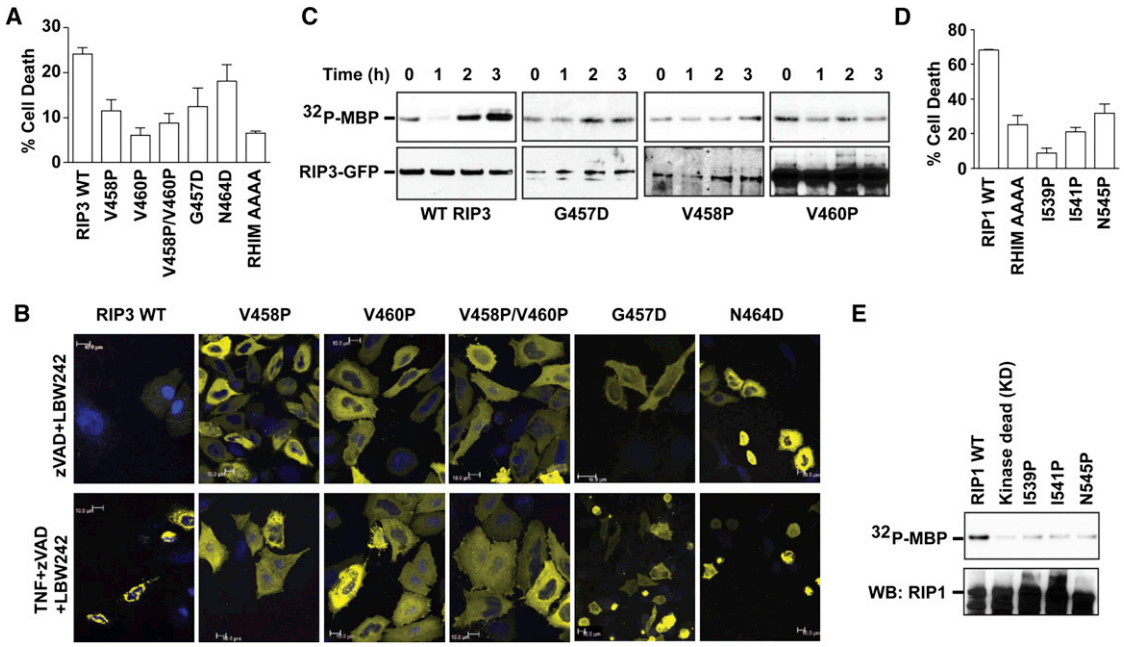

Figure 7. The RIP1/RIP3 Interaction Is Crucial for Kinase Activation, Clustering, and Cell Death

(A) Effects of RIP3 mutations on TNF-induced necrosis in HeLa cells transfected with WT or the indicated RIP3 mutants fused to YFP. AAAA, quadruple Ala mutant of RIP3 at the VQVG RHIM sequence. Results shown are averages of triplicates ±SEM.

(B) Effects of RIP3 mutations on puncta formation in HeLa cells transfected with the indicated RIP3-YFP plasmids as examined by confocal microscopy.

(C) Effects of RIP3 mutations on kinase activity of the anti-RIP3 immunoprecipitates in RIP3$^{-/-}$ fibroblasts stably expressing the indicated RIP3-GFP mutants using MBP as the substrate. Bottom panel shows the RIP3 western blot of the same membrane.

(D) Effects of RIP1 mutations on TNF-induced necrosis in RIP1$^{-/-}$ fibroblasts transfected with the indicated RIP1 fused to GFP. Results shown are averages of triplicates ±SEM.

(E) Effects of RIP1 mutations on kinase activity of the anti-GFP immunoprecipitates in 293T cells transfected with the indicated RIP1-GFP constructs using MBP as the substrate. The same membrane was probed for RIP1 on western blot in the lower panel.

See also Figure S7.

formation of neurofibrillary tangles in Alzheimer's and Parkinson's diseases, respectively, as well as in other neurodegenerative tauopathies and synucleinopathies (Avila et al., 2010; Oueslati et al., 2010). Our data are consistent with a feed-forward, gain-of-function mechanism in which kinase activation and RIP1/RIP3 necrosome formation are mutually reinforcing. In their inactive states, the core RHIM sequences may be hidden by long-range interactions in the unstructured flanking sequences of RIP1 and RIP3 and possibly by RIP1 ubiquitination. Indeed, expression of RIP1 and RIP3 RHIM fragments, but not full-length RIP1 and RIP3, induced spontaneous clustering in cells without stimulation (Figure S7B). In line with the observation of autoinhibition, it was reported that large proteins have a low propensity to form amyloid fibrils, although they possess a great tendency to form β-sheet-rich aggregates that are weak binders of ThT and CR (Ramshini et al., 2011). In contrast, the RIP1/RIP3 complex binds ThT and CR robustly, even though the folded KDs and the DD in these proteins are primarily α-helical. Kinase activation and the resultant hyperphosphorylation may be the key events that reduce this autoinhibition, perhaps as a result of charge repulsion to expose the RHIM core, leading to enhanced complex formation. In turn, complex formation further potentiates kinase activation through autophosphorylation and cross-phosphorylation, propagating the pronecrotic signal.

Is it possible that the amyloid structures per se also have toxicity to cells and contribute to cell death? It is well known that amyloids are toxic, likely as a consequence of their mass and induction of inflammation or disruption of membrane integrity (Eisenberg and Jucker, 2012). However, given that specific RIP3 kinase substrates have been identified and are crucial for induction of programmed necrosis (Sun et al., 2012; Zhao et al., 2012), kinase activation seems to be the key consequence of the formation of the RIP1/RIP3 amyloid scaffold. Drawing a parallel with the structural model of the designed amyloid of ribonuclease A (Sambashivan et al., 2005), the KDs of RIP1 and RIP3 would extend from the central amyloid spine to the periphery and find space to retain their globular structures and functions.

Previous structural studies have revealed several arrangements of cross-β amyloid spines in the formation of dry steric zippers, including those from both parallel and antiparallel β sheets (Eisenberg and Jucker, 2012; Sawaya et al., 2007). The fiber diffraction pattern of RIP1/3-RHIM (Figure 2F) showed that each β sheet in the fibrils consists of parallel β strands rather than antiparallel β strands, as evidenced by the strong 4.7 Å spacing along the fibril axis (meridional direction). Structures of related self-complementing steric zippers have also led to insights regarding complementary molecular surfaces in RIP1

and RIP3 (Sawaya et al., 2007). The core RHIM sequences of RIP1 and RIP3 and IQIG and VQVG, respectively, suggest that the hydrophobic Ile and Val residues pack to form the double β sheet in the steric zipper. This type of packing is remarkably similar to the structure of the VQIVYK sequence from tau (PDB 2ON9) (Sawaya et al., 2007), a microtubule-associated protein that plays an important role in stabilizing axonal microtubules. Particularly, the first 3 residues of the RHIM core sequences and the tau sequence are basically identical. We built two alternative models of the RHIM steric zipper based on the tau structure (Figure S7C). In both models, heterosteric zippers (Eisenberg and Jucker, 2012) for the β-amyloid spine are proposed. Notably, the hydrophobic packing between Ile and Val residues is reminiscent of tau. It is likely that packing in RIP1 or RIP3 homo-oligomeric fibrils (with Ile-Ile or Val-Val contacts) is less optimal than the Ile-Val contacts in the hetero-oligomeric complex. This preference may potentiate the unusual assembly of the RIP1/RIP3 heterodimeric complex and explain the apparent 1:1 stoichiometry between RIP1 and RIP3.

A number of additional proteins, including the cytoplasmic DNA sensor DAI, the Toll-like receptor signaling adaptor TRIF, and the murine cytomegalovirus protein M45, have been shown to contain RHIMs (Figure S7D). Both DAI and TRIF recruit RIP1 and/or RIP3 through their RHIMs to activate NF-κB or to induce cell death (Kaiser and Offermann, 2005; Meylan et al., 2004; Takaoka et al., 2007). Indeed, we show that DAI and RIP1 also form filamentous structures (Figure S7E). M45 binds to RIP1 and functions as a viral inhibitor in DNA sensing, Toll-like receptor signaling, and the TNF receptor pathway (Mack et al., 2008; Rebsamen et al., 2009; Upton et al., 2010). In all of these signaling processes, the high-order oligomeric scaffold of amyloids may be the key feature that brings signaling proteins into proximity to allow their activation. Similarly, yet distinctly, the oligomeric scaffold of the DD superfamily mediates caspase activation and apoptosis (Wang et al., 2010), as well as MyD88-dependent Toll-like receptor signaling (Lin et al., 2010). In addition, this DD superfamily scaffold exhibits functional characteristics akin to amyloids and prions in their abilities to seed and to propagate (Hou et al., 2011). For both the amyloid scaffold and the DD superfamily scaffold, the slow seeding phase and the fast growing phase in the assembly of these complexes may dictate a highly cooperative process and a digital threshold response mechanism. Assembly of highly oligomeric signalosomes may be an emerging principle in signal transduction.

EXPERIMENTAL PROCEDURES

Cloning, Protein Expression, Purification, and Mutagenesis

The RIP1 (residues 496–583)/RIP3 (residues 388–518) complex and its truncation complexes were polycistronically subcloned into the pET28a (Novagen) or pDB-His-MBP vector (Berkeley Structural Genomics Center). The RIP1 (residues 496–583) and RIP3 (residues 388–518) constructs were subcloned into the pET28a or pSMT3 vector with a His-Sumo tag. All proteins were expressed in *E. coli* BL21 (DE3) RIPL cells (Novagen) and were purified by Ni-affinity and gel filtration chromatography.

The full-length RIP1(1–671)/RIP3(1–518) complex was subcloned into pFastBacDual vector (Invitrogen) with an N-terminal His-tag on RIP1 and an N-terminal MBP-tag on RIP3. The WT and mutant RIP1 and RIP3 (RIP1-FL, RIP3-FL, RIP1-FL-I539D, and RIP3-FL-V460P) were subcloned into pFastBacHTA vector (Invitrogen) with an N-terminal His-tag. The proteins were expressed in Hi5 cells and were purified with either Ni-NTA or amylose resin followed by gel filtration chromatography.

Electron Microscopy and Image Processing

RIP1/RIP3-RHIM, RIP1-RHIM, and RIP3-RHIM were negatively stained with uranyl formate and imaged with a 1K × 1K charge-coupled device (CCD) camera (Gatan) on a CM10 electron microscope (FEI). For subsequent image processing, images were collected on imaging plates with a Tecnai T12 electron microscope. The particles were subjected to ten cycles of multireference alignment, each followed by K-means classification into 100 classes.

For full-length RIP1, RIP3, RIP1/RIP3 complex, and endogenous RIP1/3 complexes, the samples were stained using uranyl acetate and imaged with a Veleeta 2K × 2K cooled CCD camera (Olympus-Soft Imaging Solutions, Munster, Germany) on a JEM-1400 (JEOL, Ltd., Tokyo, Japan) electron microscope.

X-Ray Diffraction from Fibrils

The RIP1/RIP3-RHIM complex was dried and partially aligned by using a SpeedVac System (Savant) and mounted in a cryoloop. The diffraction image was collected by using a Rigaku RU-H3R X-ray generator on a Rigaku R-Axis IV imaging plate detector.

Congo Red Binding

CR absorption spectra were recorded from 430–600 nm in 96-well plates by using a SpectraMax M2 plate reader (Molecular Devices).

Thioflavin T Fluorescence

Fluorescence measurements were performed in 96-well plates on a SpectraMax M2 plate reader (Molecular Devices) with an excitation wavelength of 430 nm.

Circular Dichroism Spectroscopy

CD spectra of RIP1, RIP3, and the RIP1/RIP3 complex were measured on an Aviv Model 410 spectropolarimeter at a cell length of 0.1 cm at 20°C with five scans per measurement. Buffer control was subtracted from each sample spectrum.

Fourier Transform Infrared Spectroscopy

Infrared spectra were recorded by using a Bruker Tensor spectrometer (Bruker Optik, Germany) at room temperature and with a resolution of 4 cm^{-1}. The spectra represent the sum of 40 scans after reference subtraction.

Renaturation and Seeding Experiments Using ThT Fluorescence

RIP1 was denatured in 8 M urea with heating at 95°C for 10 min. The RIP1/RIP3 complex was denatured in 150 mM NaOH. The denatured proteins were diluted 100-fold into a native buffer and 50 μM ThT. The final concentration for RIP1 or the RIP1/RIP3 complex was 5μM. Seeding experiments were performed as described above with the exception that RIP1, RIP3, or RIP1/RIP3 complex seeds were added to the reaction to a final concentration of 0.5 μM. All reactions were measured kinetically at 25°C in 96-well plates with excitation and emission wavelengths of 430 nm and 485 nm, respectively.

Solid-State NMR Experiments

2D DARR spectra were recorded on a Bruker Advance III 400 spectrometer. The 2D ^{13}C-^{13}C DARR and DREAM spectra used for the resonance assignment, as well as the 1D ^{13}C spectra, were recorded on an Advance II 900 spectrometer. Data were collected at ~10°C if not mentioned otherwise. All triple resonance spectra used for the assignment were recorded on an Advance I 750 spectrometer. All spectra were processed by using Topspin 3.1 and analyzed using the program CARA.

Confocal Microscopy

For ThT staining, HeLa cells were plated on coverslips and transfected with RIP3-mCherry. After 15–18 hr, cells were treated with zVAD-fmk, LBW242, and TNF for 3 hr. 20 μM ThT was added to cells 1 hr prior to fixation and imaging with a Leica SP5 confocal microscope. For microscopy of WT and

mutant RIP1-CFP, RIP1-GFP, or RIP3-YFP, transfected NIH 3T3 fibroblasts or HeLa cells were induced to undergo necrosis and visualized by confocal microscopy.

Cell Death Assays

For inhibition of programmed necrosis, CR, ThT, or HBX were used at the indicated concentrations on HT-29 cells treated with TNF, LBW242, and zVAD-fmk. Cell death was determined by lactate dehydrogenase (LDH) release or propidium iodide (PI) exclusion using flow cytometry. For induction of apoptosis, HT-29 cells were pretreated with the indicated concentrations of inhibitors prior to stimulation with IFN-γ and anti-Fas antibody.

For effects of RIP3 mutations, HeLa cells were transfected with WT or mutant RIP3 fused to YFP. Cells were treated with zVAD-fmk, LBW242, and TNF, and cell death was determined in the YFP-positive population with PI by flow cytometry. For effects of RIP1 mutations, RIP1$^{-/-}$ fibroblasts were transfected with WT or mutant RIP1 fused to GFP. Cells were similarly treated, and cell death was determined in the GFP-positive population by PI flow cytometry.

ThT Binding and Immunogold EM of the Endogenous RIP1/RIP3 Complex

RIP1 immunoprecipitates were purified from necrotic HT-29 cells, and ThT fluorescence was measured from 450–550 nm by using a Spex Fluorolog-3 spectrofluorometer with excitation at 430 nm. For immunogold EM analyses, necrotic MEFs were fixed in 4% paraformaldehyde. RIP1 (BD PharMingen) and RIP3 (ProSci) antibodies were applied at 1:50 dilutions. Secondary immunogold conjugated antibodies (15 nm for RIP1 and 6 nm for RIP3) were used at 1:50 dilution.

Stability Assessment of the Endogenous RIP1/RIP3 Complex

HT-29 cells were lysed in lysis buffer supplemented with 4 M urea, 8 M urea, or 150 mM NaOH. Thirty minutes after lysis, cell lysates were diluted 10-fold with regular lysis buffer and immunoprecipitated with anti-RIP3 antibody. For TNFR1 complexes, WT MEFs were treated with TNF for 2 min. Cell lysis was performed as for the RIP1/RIP3 complexes.

In Vitro Kinase Assays

293T cells were transfected with indicated RIP1 or RIP3 mutants fused to GFP or YFP, respectively. The fusion proteins were immunoprecipitated 24 hr later with anti-GFP antibody (Roche). For RIP3 stable fibroblasts, RIP3 complexes were immunoprecipitated after necrosis induction. The resulting immune complexes were used for in vitro kinase assay using myelin basic protein (MBP, Stressgen) as substrate.

SUPPLEMENTAL INFORMATION

Supplemental Information includes Extended Experimental Procedures and seven figures and can be found with this article online at http://dx.doi.org/10.1016/j.cell.2012.06.019.

ACKNOWLEDGMENTS

We thank L. Cohen-Gould for help with EM imaging at the Weill Cornell Microscopy Facility, S.M. Damo for initial work on this project, Q. Li for insect cell expression, V. Kumar for ThT measurement of endogenous complexes, and D. Porter (Novartis) for the generous gift of LBW242. This work was supported by grants to F.K.C. (AI083497 and AI088502) and H.W. (AI045937). F.K.C. is a member of the UMass DERC (DK32520). J.N. is an Irvington Institute postdoctoral fellow of the Cancer Research Institute, and D.M. is supported by NIH training grant T32 AI07349. T.W. is an investigator in the Howard Hughes Medical Institute.

Received: April 6, 2012
Revised: May 7, 2012
Accepted: June 8, 2012
Published: July 19, 2012

REFERENCES

Alavez, S., Vantipalli, M.C., Zucker, D.J., Klang, I.M., and Lithgow, G.J. (2011). Amyloid-binding compounds maintain protein homeostasis during ageing and extend lifespan. Nature *472*, 226–229.

Avila, J., Gómez de Barreda, E., Engel, T., Lucas, J.J., and Hernández, F. (2010). Tau phosphorylation in hippocampus results in toxic gain-of-function. Biochem. Soc. Trans. *38*, 977–980.

Balbirnie, M., Grothe, R., and Eisenberg, D.S. (2001). An amyloid-forming peptide from the yeast prion Sup35 reveals a dehydrated beta-sheet structure for amyloid. Proc. Natl. Acad. Sci. USA *98*, 2375–2380.

Challa, S., Woelfel, M., Guildford, M., Moquin, D., and Chan, F.K. (2010). Viral cell death inhibitor MC159 enhances innate immunity against vaccinia virus infection. J. Virol. *84*, 10467–10476.

Chan, F.K., Shisler, J., Bixby, J.G., Felices, M., Zheng, L., Appel, M., Orenstein, J., Moss, B., and Lenardo, M.J. (2003). A role for tumor necrosis factor receptor-2 and receptor-interacting protein in programmed necrosis and antiviral responses. J. Biol. Chem. *278*, 51613–51621.

Chiti, F., and Dobson, C.M. (2006). Protein misfolding, functional amyloid, and human disease. Annu. Rev. Biochem. *75*, 333–366.

Cho, Y.S., Challa, S., Moquin, D., Genga, R., Ray, T.D., Guildford, M., and Chan, F.K. (2009). Phosphorylation-driven assembly of the RIP1-RIP3 complex regulates programmed necrosis and virus-induced inflammation. Cell *137*, 1112–1123.

Cho, Y., McQuade, T., Zhang, H., Zhang, J., and Chan, F.K. (2011). RIP1-dependent and independent effects of necrostatin-1 in necrosis and T cell activation. PLoS ONE *6*, e23209.

Detken, A., Hardy, E.H., Ernst, M., and Meier, B.H. (2002). Simple and efficient decoupling in magic-angle spinning solid-state NMR: the XiX scheme. Chem. Phys. Lett. *356*, 298–304.

Eisenberg, D., and Jucker, M. (2012). The amyloid state of proteins in human diseases. Cell *148*, 1188–1203.

Feng, S., Yang, Y., Mei, Y., Ma, L., Zhu, D.E., Hoti, N., Castanares, M., and Wu, M. (2007). Cleavage of RIP3 inactivates its caspase-independent apoptosis pathway by removal of kinase domain. Cell. Signal. *19*, 2056–2067.

Feoktistova, M., Geserick, P., Kellert, B., Dimitrova, D.P., Langlais, C., Hupe, M., Cain, K., MacFarlane, M., Häcker, G., and Leverkus, M. (2011). cIAPs block Ripoptosome formation, a RIP1/caspase-8 containing intracellular cell death complex differentially regulated by cFLIP isoforms. Mol. Cell *43*, 449–463.

Frank, J., Radermacher, M., Penczek, P., Zhu, J., Li, Y., Ladjadj, M., and Leith, A. (1996). SPIDER and WEB: processing and visualization of images in 3D electron microscopy and related fields. J. Struct. Biol. *116*, 190–199.

Gaither, A., Porter, D., Yao, Y., Borawski, J., Yang, G., Donovan, J., Sage, D., Slisz, J., Tran, M., Straub, C., et al. (2007). A Smac mimetic rescue screen reveals roles for inhibitor of apoptosis proteins in tumor necrosis factor-alpha signaling. Cancer Res. *67*, 11493–11498.

He, S., Wang, L., Miao, L., Wang, T., Du, F., Zhao, L., and Wang, X. (2009). Receptor interacting protein kinase-3 determines cellular necrotic response to TNF-alpha. Cell *137*, 1100–1111.

He, S., Liang, Y., Shao, F., and Wang, X. (2011). Toll-like receptors activate programmed necrosis in macrophages through a receptor-interacting kinase-3-mediated pathway. Proc. Natl. Acad. Sci. USA *108*, 20054–20059.

Hou, F., Sun, L., Zheng, H., Skaug, B., Jiang, Q.X., and Chen, Z.J. (2011). MAVS forms functional prion-like aggregates to activate and propagate antiviral innate immune response. Cell *146*, 448–461.

Kaiser, W.J., and Offermann, M.K. (2005). Apoptosis induced by the toll-like receptor adaptor TRIF is dependent on its receptor interacting protein homotypic interaction motif. J. Immunol. *174*, 4942–4952.

Kaiser, W.J., Upton, J.W., Long, A.B., Livingston-Rosanoff, D., Daley-Bauer, L.P., Hakem, R., Caspary, T., and Mocarski, E.S. (2011). RIP3 mediates the embryonic lethality of caspase-8-deficient mice. Nature *471*, 368–372.

Klunk, W.E., Pettegrew, J.W., and Abraham, D.J. (1989). Quantitative evaluation of congo red binding to amyloid-like proteins with a beta-pleated sheet conformation. J. Histochem. Cytochem. *37*, 1273–1281.

LeVine, H., III. (1999). Quantification of beta-sheet amyloid fibril structures with thioflavin T. Methods Enzymol. *309*, 274–284.

Li, Z., Hite, R.K., Cheng, Y., and Walz, T. (2010). Evaluation of imaging plates as recording medium for images of negatively stained single particles and electron diffraction patterns of two-dimensional crystals. J. Electron Microsc. (Tokyo) *59*, 53–63.

Lin, Y., Devin, A., Rodriguez, Y., and Liu, Z.G. (1999). Cleavage of the death domain kinase RIP by caspase-8 prompts TNF-induced apoptosis. Genes Dev. *13*, 2514–2526.

Lin, S.C., Lo, Y.C., and Wu, H. (2010). Helical assembly in the MyD88-IRAK4-IRAK2 complex in TLR/IL-1R signalling. Nature *465*, 885–890.

Ludtke, S.J., Baldwin, P.R., and Chiu, W. (1999). EMAN: semiautomated software for high-resolution single-particle reconstructions. J. Struct. Biol. *128*, 82–97.

Mack, C., Sickmann, A., Lembo, D., and Brune, W. (2008). Inhibition of proinflammatory and innate immune signaling pathways by a cytomegalovirus RIP1-interacting protein. Proc. Natl. Acad. Sci. USA *105*, 3094–3099.

Meng, F., Abedini, A., Plesner, A., Verchere, C.B., and Raleigh, D.P. (2010). The flavanol (-)-epigallocatechin 3-gallate inhibits amyloid formation by islet amyloid polypeptide, disaggregates amyloid fibrils, and protects cultured cells against IAPP-induced toxicity. Biochemistry *49*, 8127–8133.

Meylan, E., Burns, K., Hofmann, K., Blancheteau, V., Martinon, F., Kelliher, M., and Tschopp, J. (2004). RIP1 is an essential mediator of Toll-like receptor 3-induced NF-kappa B activation. Nat. Immunol. *5*, 503–507.

Moquin, D., and Chan, F.K. (2010). The molecular regulation of programmed necrotic cell injury. Trends Biochem. Sci. *35*, 434–441.

Oberst, A., Dillon, C.P., Weinlich, R., McCormick, L.L., Fitzgerald, P., Pop, C., Hakem, R., Salvesen, G.S., and Green, D.R. (2011). Catalytic activity of the caspase-8-FLIP(L) complex inhibits RIPK3-dependent necrosis. Nature *471*, 363–367.

Oueslati, A., Fournier, M., and Lashuel, H.A. (2010). Role of post-translational modifications in modulating the structure, function and toxicity of alpha-synuclein: implications for Parkinson's disease pathogenesis and therapies. Prog. Brain Res. *183*, 115–145.

Ramshini, H., Parrini, C., Relini, A., Zampagni, M., Mannini, B., Pesce, A., Saboury, A.A., Nemat-Gorgani, M., and Chiti, F. (2011). Large proteins have a great tendency to aggregate but a low propensity to form amyloid fibrils. PLoS ONE *6*, e16075.

Rebsamen, M., Heinz, L.X., Meylan, E., Michallet, M.C., Schroder, K., Hofmann, K., Vazquez, J., Benedict, C.A., and Tschopp, J. (2009). DAI/ZBP1 recruits RIP1 and RIP3 through RIP homotypic interaction motifs to activate NF-kappaB. EMBO Rep. *10*, 916–922.

Rost, B., Yachdav, G., and Liu, J. (2004). The PredictProtein server. Nucleic Acids Res. *32*, W321–W326.

Sambashivan, S., Liu, Y., Sawaya, M.R., Gingery, M., and Eisenberg, D. (2005). Amyloid-like fibrils of ribonuclease A with three-dimensional domain-swapped and native-like structure. Nature *437*, 266–269.

Sánchez, I., Mahlke, C., and Yuan, J. (2003). Pivotal role of oligomerization in expanded polyglutamine neurodegenerative disorders. Nature *421*, 373–379.

Sawaya, M.R., Sambashivan, S., Nelson, R., Ivanova, M.I., Sievers, S.A., Apostol, M.I., Thompson, M.J., Balbirnie, M., Wiltzius, J.J., McFarlane, H.T., et al. (2007). Atomic structures of amyloid cross-beta spines reveal varied steric zippers. Nature *447*, 453–457.

Stanger, B.Z., Leder, P., Lee, T.H., Kim, E., and Seed, B. (1995). RIP: a novel protein containing a death domain that interacts with Fas/APO-1 (CD95) in yeast and causes cell death. Cell *81*, 513–523.

Sun, X., Lee, J., Navas, T., Baldwin, D.T., Stewart, T.A., and Dixit, V.M. (1999). RIP3, a novel apoptosis-inducing kinase. J. Biol. Chem. *274*, 16871–16875.

Sun, X., Yin, J., Starovasnik, M.A., Fairbrother, W.J., and Dixit, V.M. (2002). Identification of a novel homotypic interaction motif required for the phosphorylation of receptor-interacting protein (RIP) by RIP3. J. Biol. Chem. *277*, 9505–9511.

Sun, L., Wang, H., Wang, Z., He, S., Chen, S., Liao, D., Wang, L., Yan, J., Liu, W., Lei, X., and Wang, X. (2012). Mixed lineage kinase domain-like protein mediates necrosis signaling downstream of RIP3 kinase. Cell *148*, 213–227.

Sunde, M., Serpell, L.C., Bartlam, M., Fraser, P.E., Pepys, M.B., and Blake, C.C. (1997). Common core structure of amyloid fibrils by synchrotron X-ray diffraction. J. Mol. Biol. *273*, 729–739.

Takaoka, A., Wang, Z., Choi, M.K., Yanai, H., Negishi, H., Ban, T., Lu, Y., Miyagishi, M., Kodama, T., Honda, K., et al. (2007). DAI (DLM-1/ZBP1) is a cytosolic DNA sensor and an activator of innate immune response. Nature *448*, 501–505.

Takegoshi, K., Nakamura, S., and Terao, T. (2001). ^{13}C–^{1}H dipolar-assisted rotational resonance in magic-angle spinning NMR. Chem. Phys. Lett. *344*, 631–637.

Tenev, T., Bianchi, K., Darding, M., Broemer, M., Langlais, C., Wallberg, F., Zachariou, A., Lopez, J., MacFarlane, M., Cain, K., and Meier, P. (2011). The Ripoptosome, a signaling platform that assembles in response to genotoxic stress and loss of IAPs. Mol. Cell *43*, 432–448.

Uptain, S.M., and Lindquist, S. (2002). Prions as protein-based genetic elements. Annu. Rev. Microbiol. *56*, 703–741.

Upton, J.W., Kaiser, W.J., and Mocarski, E.S. (2010). Virus inhibition of RIP3-dependent necrosis. Cell Host Microbe *7*, 302–313.

Upton, J.W., Kaiser, W.J., and Mocarski, E.S. (2012). DAI/ZBP1/DLM-1 complexes with RIP3 to mediate virus-induced programmed necrosis that is targeted by murine cytomegalovirus vIRA. Cell Host Microbe *11*, 290–297.

Verel, R., Ernst, M., and Meier, B.H. (2001). Adiabatic dipolar recoupling in solid-state NMR: the DREAM scheme. J. Magn. Reson. *150*, 81–99.

Walczak, H. (2011). TNF and ubiquitin at the crossroads of gene activation, cell death, inflammation, and cancer. Immunol. Rev. *244*, 9–28.

Wang, L., Du, F., and Wang, X. (2008). TNF-alpha induces two distinct caspase-8 activation pathways. Cell *133*, 693–703.

Wang, L., Yang, J.K., Kabaleeswaran, V., Rice, A.J., Cruz, A.C., Park, A.Y., Yin, Q., Damko, E., Jang, S.B., Raunser, S., et al. (2010). The Fas-FADD death domain complex structure reveals the basis of DISC assembly and disease mutations. Nat. Struct. Mol. Biol. *17*, 1324–1329.

Welz, P.S., Wullaert, A., Vlantis, K., Kondylis, V., Fernández-Majada, V., Ermolaeva, M., Kirsch, P., Sterner-Kock, A., van Loo, G., and Pasparakis, M. (2011). FADD prevents RIP3-mediated epithelial cell necrosis and chronic intestinal inflammation. Nature *477*, 330–334.

Whitmore, L., and Wallace, B.A. (2004). DICHROWEB, an online server for protein secondary structure analyses from circular dichroism spectroscopic data. Nucleic Acids Res. *32*(Web Server issue), W668–W673.

Yu, P.W., Huang, B.C., Shen, M., Quast, J., Chan, E., Xu, X., Nolan, G.P., Payan, D.G., and Luo, Y. (1999). Identification of RIP3, a RIP-like kinase that activates apoptosis and NFkappaB. Curr. Biol. *9*, 539–542.

Zandomeneghi, G., Krebs, M.R., McCammon, M.G., and Fändrich, M. (2004). FTIR reveals structural differences between native beta-sheet proteins and amyloid fibrils. Protein Sci. *13*, 3314–3321.

Zhang, D.W., Shao, J., Lin, J., Zhang, N., Lu, B.J., Lin, S.C., Dong, M.Q., and Han, J. (2009). RIP3, an energy metabolism regulator that switches TNF-induced cell death from apoptosis to necrosis. Science *325*, 332–336.

Zhang, H., Zhou, X., McQuade, T., Li, J., Chan, F.K., and Zhang, J. (2011). Functional complementation between FADD and RIP1 in embryos and lymphocytes. Nature *471*, 373–376.

Zhao, J., Jitkaew, S., Cai, Z., Choksi, S., Li, Q., Luo, J., and Liu, Z.G. (2012). Mixed lineage kinase domain-like is a key receptor interacting protein 3 downstream component of TNF-induced necrosis. Proc. Natl. Acad. Sci. U S A.

EXTENDED EXPERIMENTAL PROCEDURES

Cloning, Protein Expression, Purification, and Mutagenesis

The RIP1 (residues 496–583)/RIP3 (residues 388–518) complex and its truncation complexes were polycistronically subcloned into the pET28a (Novagen) or pDB-His-MBP vector (Berkeley Structural Genomics Center). The RIP1 (residues 496–583) and RIP3 (residues 388–518) alone constructs were subcloned into the pET28a or pSMT3 vector with a His-Sumo tag. All proteins with N-terminal His-tags were expressed in *E. coli* BL21 (DE3) RIPL cells (Novagen). Bacterial cells were transformed with expression plasmids and grown in Luria broth supplemented with 40 μg/ml kanamycin and 25 μg/ml chloramphenicol. At an OD600 of 0.6, protein expression was induced with 0.5 mM isopropyl β-D-thiogalactoside (Fisher Scientific). After 18 hr of induction at 20°C, cells were harvested by centrifugation at 5,000 rpm for 10 min and lysed by sonication or high pressure in a buffer containing 50 mM Tris-HCl (pH8.0), 300 mM NaCl, 1 mM phenylmethylsulfonyl fluoride, 1 mM β-mercaptoethanol and a protease inhibitor cocktail (Roche). After spinning at 16,000 rpm for 50 min, the supernatant was incubated with Ni-NTA agarose (QIAGEN) at 4°C for 60 min. The subsequent purification procedure followed the standard manual from QIAGEN. The protein was further purified by gel filtration chromatography using the Superdex 200 10/300 GL column (GE Healthcare) and an ÄKTAFPLC (GE Healthcare) at either 4°C or room temperature with a running buffer of 20 mM Tris-HCl (pH 7.4), 150 mM NaCl, and 2 mM dithiothreitol. The purified protein was concentrated to 5 mg/ml, flash-frozen in liquid nitrogen and stored at −80°C. Protein concentrations were determined by the Bradford assay using BSA as a standard.

The full-length RIP1(1-671)/RIP3(1-518) complex was subcloned into pFastBacDual vector (Invitrogen) with an N-terminal His-tag on RIP1 and an N-terminal MBP-tag on RIP3. The WT and mutant RIP1 and RIP3 (RIP1-FL, RIP3-FL, RIP1-FL-I539D, and RIP3-FL-V460P) were subcloned into pFastBacHTA vector (Invitrogen) with an N-terminal His-tag. Baculoviruses were generated in DH10BAC cells, amplified, and used to infect Hi5 insect cells in serum-free media (Invitrogen). The cells were cultured in suspension and harvested 48 hr post-infection. WT and mutant RIP1-FL and RIP3-FL were purified with Ni-NTA agarose following the standard manual from QIAGEN. RIP1/RIP3-FL was purified by amylose resin with the standard manual from NEB followed by gel filtration chromatography using the Superdex 200 10/300 GL column (GE Healthcare). All mutagenesis was performed according to the QuikChange site-directed mutagenesis kit protocol (Stratagene).

Electron Microscopy and Image Processing

RIP1/RIP3-RHIM, RIP1-RHIM and RIP3-RHIM were negatively stained with uranyl formate, and imaged with a 1K × 1K CCD camera (Gatan) on a CM10 electron microscope (FEI). For subsequent image processing, images were collected on imaging plates with a Tecnai T12 electron microscope equipped with an LaB6 filament, operated at 120 kV, and using a defocus of –1.5 μm. Imaging plates were read out with a DITABIS scanner (Digital Biomedical Imaging System AG) using a step size of 15 μm, a gain setting of 20,000, and a laser power setting of 30%; 2 × 2 pixels were averaged to yield a pixel size of 4.5 Å at the specimen level (Li et al., 2010). Using BOXER, the display program associated with the EMAN software package (Ludtke et al., 1999), a total of 11,406 areas of RIP1/RIP3 fibrils were selected from 77 images. Using the SPIDER software package (Frank et al., 1996), the particles were windowed into 60 × 60 pixel images, rotationally and translationally aligned, and subjected to 10 cycles of multi-reference alignment. Each round of multi-reference alignment was followed by K-means classification into 100 classes. The references used for the first multi-reference alignment were randomly chosen from the particle images.

For full-length RIP1, RIP3, RIP1/RIP3 complex, and endogenous RIP1/3 complexes, the samples were stained using uranyl acetate. Briefly, protein samples (5 μl) were applied to formvar/carbon-coated grids and allowed to adsorb for 1 min. Excess liquid was blotted off, and a drop of 1.5% uranyl acetate was applied. Excess liquid was blotted off again, and staining was repeated for a total of 4 times. The grids were then allowed to air dry. The grids were examined and imaged in a JEM-1400 (JEOL, Ltd., Tokyo, Japan) electron microscope, operated at 80 kV. 16-bit Images were captured with a Veleeta 2K x 2K cooled CCD camera (Olympus-Soft Imaging Solutions, Munster, Germany).

X-Ray Diffraction from Fibrils

A 2 mg/ml solution of the RIP1/RIP3 complex was dried using a SpeedVac System (Savant). Dried and partially aligned fibrils were mounted in a cryo-loop and exposed to Cu Kα radiation from a Rigaku RU-H3R X-ray generator operating at 50 kV and 100 mA. Data were collected at room temperature for 30 min with a 5° oscillation on a Rigaku R-Axis IV imaging plate detector.

Congo Red Binding

Congo red (CR) binding was detected using a previously described method (Klunk et al., 1989) at 25°C in 96-well plates using a SpectraMax M2 plate reader (Molecular Devices). The incubation time with CR was 1 hr at room temperature and the concentration of CR was 15 μM.

Thioflavin T Fluorescence

Fluorescence measurements were performed similarly as described previously (Meng et al., 2010) at 25°C in 96-well plates on a SpectraMax M2 plate reader (Molecular Devices) with an excitation wavelength of 430 nm. The final ThT concentrations ranged from 10-100 μM in 20 mM Tris-HCl (pH 7.5).

Circular Dichroism Spectroscopy

Samples containing 20 μM RIP1, RIP3, or the RIP1/RIP3 complex, supplied in 20 mM Tris-HCl (pH 7.4), 150 mM NaCl, and 2 mM dithiothreitol, were measured on a Aviv Model 410 spectropolarimeter at a cell length of 0.1 cm at 20°C, using 1 nm/second scanning speed, 1 s response time, and 5 scans per measurement. Buffer control was subtracted from each sample spectrum.

Fourier Transform Infrared Spectroscopy

Infrared spectra were recorded at room temperature with a resolution of 4 cm^{-1} using a Bruker Tensor spectrometer (Bruker Optik, Germany) equipped with a BIO-ATR II cell and a LN-MCT Photovoltaic detector. The spectra represent the sum of 40 scans after reference subtraction. The proteins were in 20 mM Tris-HCl (pH 7.4), 150 mM NaCl, and 2 mM dithiothreitol at 0.5∼2 mg/ml concentration.

Renaturation and Seeding Experiments Using ThT Fluorescence

RIP1 was denatured in a buffer containing 8 M urea, 100 mM NaCl, 20 mM Tris-HCl (pH 7.5), followed by heating at 95þC for 10 min. The RIP1/RIP3 complex was denatured by adding NaOH to a final concentration of 150 mM. The denatured proteins were diluted 100-fold into a buffer containing 100 mM NaCl, 20 mM Tris-HCl (pH 7.5) and 50 μM ThT. The final concentration for RIP1 or the RIP1/RIP3 complex was 5μM. Seeding experiments were performed as described above with the exception that RIP1, RIP3 or RIP1/RIP3 complex seeds were added to the reaction to a final concentration of 0.5 μM. All reactions were measured kinetically at 25°C in 96-well plates with excitation and emission wavelengths of 430 nm and 485 nm, respectively.

Solid-State NMR Experiments

For all solid-state NMR experiments, the ^{1}H and ^{13}C hard pulse radio frequency (rf) field strengths were 100 kHz and 50 kHz, respectively. The Hartman-Hahn cross polarizations (CP) were done with a ^{13}C rf-field strength of 50 kHz and adjusting the ^{1}H rf-field strength to the n = 1 Hartman-Hahn condition. 2D DARR (Takegoshi et al., 2001) spectra were recorded on a Bruker Advance III 400 spectrometer equipped with a 3.2 mm probe operating at 20 kHz MAS. The sweep width was 25 kHz in both dimensions and 32 free induction decays (FIDs) (48 for the RIP1 (residues 496-583)/RIP3 (residues 446-518) complex) were recorded for every one of the 500 indirect t_1 increments. The 2D ^{13}C-^{13}C DARR and DREAM spectra (Verel et al., 2001) used for the resonance assignment as well as the 1D ^{13}C spectra were recorded on an Advance II 900 spectrometer using a 3.2 mm E-free probe operating at 20 kHz MAS. The sweep width was 56 kHz in both dimensions and 16 FIDs were recorded for each t_1 increment (1024 for DARR, 768 for DREAM). The mixing times for the DARR and DREAM spectra were 100 ms and 2 ms, respectively. XiX (Detken et al., 2002) decoupling was employed during t_1 and t_2, and continuous wave (cw) decoupling was used during the DREAM mixing, both with an rf-field strength of 80 kHz. Data were collected at ∼10°C if not mentioned otherwise.

All triple resonance spectra used for the assignment were recorded on an Advance I 750 spectrometer using a 3.2 mm HCN probe operating at 16 kHz MAS. ^{15}N hard pulses were done with an rf-field strength of 40 kHz and the ^{1}H-^{15}N CP was done using 40 kHz and 56 kHz on ^{1}H and ^{15}N respectively. For the N-C′ cross polarization, we used a mixing time of 6 ms and rf-field strengths of 4 kHz and 20 kHz on ^{13}C and ^{15}N, respectively. For the N-C^{α} CP we used a mixing time of 4 ms and rf-field strengths of 56 kHz and 40 kHz, respectively. For the NCA and NCO experiments, we recorded 128 FIDs for each of the 80 indirect t_1 increments and used sweep widths of 56 kHz and 5 kHz for ^{13}C and ^{15}N, respectively. The NCACX experiment was done similarly to the NCA experiment with an additional DREAM mixing sequence of 2 ms. For the truncated NcaCX 2D experiment, we recorded 896 FIDs for each of the 60 indirect t_1 increments and used sweep widths of 56 kHz and 5 kHz for ^{13}C and ^{15}N, respectively. The 3D NCACX experiment was recorded with 48 FIDs for each of the 40 indirect t_2 (^{13}C) and 25 (^{15}N) t_1 increments. The sweep widths were 56 kHz, 7 kHz, and 4 kHz, for t_3, t_2, and t_1 respectively.

The NCOCX experiment was done similarly to the NCO experiment with an additional DARR mixing sequence of 50 ms. For the truncated NcoCX 2D experiment, we recorded 384 FIDs for each of the 80 indirect t_1 increments and used a sweep width of 56 kHz and 5 kHz for ^{13}C and ^{15}N, respectively. The 3D NCOCX experiment was recorded with 48 FIDs for each of the 32 indirect t_2 (^{13}C) and 40 (^{15}N) t_1 increments. The sweep widths were 56 kHz, 4 kHz, and 5 kHz, for t_3, t_2, and t_1 respectively. TPPM (Bennett et al., 1995) decoupling with an rf-field strength of 80 kHz was employed during t_1 and t_2, and 100 kHz cw decoupling was used during the DREAM mixing and ^{15}N-^{13}C CP. All spectra were processed using Topspin 3.1 and analyzed using the program CARA.

Confocal Microscopy

For ThT staining, HeLa cells were plated on coverslips at 250,000 cells/ml on 24-well plates and transfected with 0.5 mg hRIP3-mCherry using Fugene HD (Promega) per manufacturer's protocol. After 15-18 hr, cells were pretreated with 10 μM zVAD-fmk, 5 μM LBW242 (Gaither et al., 2007) (kind gift from Novartis), and 20 μM ThT for 1 hr prior to stimulation with 20 ng/ml hTNF. Three hours later, cells were fixed with 2% paraformaldehyde for 30 min, permeabilized with 0.05% Triton X-100, and mounted on slides with Prolong Antifade (Invitrogen). Images were captured using a Leica SP5 confocal microscope with a 63X objective.

For microscopy of WT and mutant RIP1-CFP, RIP1-GFP or RIP3-YFP, NIH 3T3 fibroblasts or HeLa cells were transfected with Fugene HD per manufacturer's protocol. Sixteen hours later, cells were pre-treated with 10 mM zVAD-fmk and 5 mM LBW242 for 1 hr prior to stimulation with TNF and visualization by confocal microscopy. All mutants were sequenced to confirm the sequence integrity.

Cell Death Assays

For inhibition of programmed necrosis, Congo red, ThT or HBX was used at the indicated concentrations on HT-29 cells treated with 100 ng/ml hTNF, 10 μM LBW242, and 20 μM zVAD-fmk. Cell death was determined by LDH release assay after 16 hr or by flow cytometry using propidium iodide (PI) exclusion as an indicator of cell death. For induction of apoptosis, HT29 cells (20,000 cells/well) were either pretreated with the indicated concentrations of inhibitors prior to stimulation with 250 units/ml IFN-γ and 0.25 μg/ml anti-Fas antibody (clone CH11) for 36 hr. Cell death was measured by MTS and LDH release assays (Promega). For Congo red inhibition, cell death was measured by flow cytometry using PI as an indicator of cell death.

For transfection of WT or mutant RIP3 fused to YFP, HeLa cells were transfected with Fugene HD per manufacturer's instructions. Eighteen hours later, cells were treated with 10 μM zVAD-fmk, 5 μM LBW242 and 20 ng/ml hTNF. Cell death was determined in the YFP positive population 14 hr later with PI by flow cytometry.

RIP1$^{-/-}$ fibroblasts were used to test the effects of RIP1 mutants in necrosis. Transfection of fibroblasts was performed using Fugene HD. Fibroblasts were treated with 10 μM zVAD-fmk, 5 μM LBW242 and 1 ng/ml mTNF for 6 hr prior to enumeration of cell death by flow cytometry. Necrosis was induced with 100 ng/ml hTNF, 20 μM zVAD-fmk and 5 μM LBW242. Cell death was determined by PI exclusion using a BD LSR2 flow cytometer. Cell death was calculated as described before (Challa et al., 2010).

ThT Binding and Immunogold EM of the Endogenous RIP1/RIP3 Complex

For immunoprecipitations, ~300 million HT-29 cells were treated with 100 ng/ml human TNF, 20 μM zVAD-fmk, and 10 μM LBW242 for 8 hr. RIP1 complex was purified as described before (Cho et al., 2009). The resulting protein complex was eluted from the beads with low pH elution buffer (Thermo Scientific), followed by neutralization with 1/10 volume of 1 M Tris-HCl (pH 8.0). For ThT fluorimetry, the RIP1 complexes were resuspended in 20 mM Tris-HCl (pH7.5) containing 50 μM ThT. ThT fluorescence was measured using a Spex Fluorolog-3 spectrofluorometer with T-format dual detection channels and Glan-Thompson polarizers. Excitation was performed at 430 nm and emission was measured from 450 to 550 nm.

For immunogold EM analyses, MEFs were stimulated with 10 μM zVAD-fmk and 1 ng/ml mTNF and fixed in 4% paraformaldehyde. RIP1 (BD PharMingen) and RIP3 (ProSci) antibodies were applied at 1:50 dilutions. Secondary immunogold conjugated antibodies (15 nm for RIP1 and 6 nm for RIP3) were used at 1:50 dilution.

Stability Assessment of the Endogenous RIP1/RIP3 Complex

HT-29 cells were treated with 100 ng/ml TNF, 20 μM zVAD-fmk and 5 μM LBW242 for 8 hr. Cells were lysed in lysis buffer containing 20 mM Tris-HCl, pH 7.4, 150 mM NaCl, 0.2% NP-40, 1 mM EDTA, 1 mM NaF, 1 mM β-glycerophosphate, 10% glycerol, and complete protease inhibitor (Roche) and phosphastase inhibitor (Sigma) cocktails, supplemented with 4 M urea, 8 M urea, or 150 mM NaOH. Thirty minutes after lysis, cell lysates were diluted ten-fold with lysis buffer without urea or NaOH. After pre-clearing with Sepharose 6B beads, the lysates were immunoprecipitated with anti-RIP3 antibody for 4 hr, washed and resolved on SDS-PAGE. For TNFR1 complexes, wild-type MEFs were treated with 20 ng/ml mouse TNF for 2 min. Cell lysis was performed as for the RIP1/RIP3 complexes.

In Vitro Kinase Assays

293T cells were transfected with indicated RIP1 or RIP3 mutants fused to GFP or YFP, respectively. Twenty-four hours later, the fusion proteins were immunoprecipitated with anti-GFP antibody (Roche). For RIP3 stable fibroblasts, 3.5 million cells were stimulated with 100 ng/ml TNF and 20 μM zVAD-fmk for the indicated times and RIP3 complexes were immunoprecipitated with anti-RIP3 antibody. The resulting immune complexes were used for in vitro kinase assay in kinase buffer (20 mM HEPES pH 7.5, 2 mM DTT, 1 mM NaF, 1 mM Na_3VO_4, 20 mM β-glycerophosphate, 20 mM $MgCl_2$, 20 mM $MnCl_2$, 1 mM EDTA, 100 μM cold ATP and 10 μCi of γ-^{32}P-ATP) supplemented with 5 μg of myelin basic protein (MBP, Stressgen) for 30 min at 30°C. Reactions were quenched by boiling in sample loading buffer. Western blots were performed as described previously (Cho et al., 2011).

SUPPLEMENTAL REFERENCE

Bennett, A.E., Rienstra, C.M., Auger, M., Lakshmi, K.V., and Griffin, R.G. (1995). Heteronuclear decoupling in rotating solids. J. Chem. Phys. *103*, 6951–6958.

A

```
                                                  :*:*   *
                                                  IQIG   N
hsRIP1  512-571  GNTPTMPFSSLPPTDESIKYTIYNSTGIQIGAYNYMEIGGTSSSLLDSTNTNFKEEPAAK
mfRIP1  447-506  GNTPTMPFTSLPLTDESIKYAIYNSTGIQIGAYNYMEVGGTSSSLLDSTNTNFKEEPASK
mmRIP1  512-571  GNTPTMPFTSLPLTDESIKYAIYNSTGIQIGAYNYMEVGGTSSSLLDSTNTNFKEEPASK
cjRIP1  511-570  GNTPTMPFSSLPLPEESIKCTIHNSSGVQIGAYNYMEVGGMSSSLSDSINMNFKEEPASK
ecRIP1  511-570  GNTPTIPFISFPSRDESAKYTICNSTGIQIGHYNYMEIGGMTSQLLDGTYMNLKQEPASK
btRIP1  506-565  GNTPTIPFTSLPSRDESSKYTIHSSSGIQIGDSNYMEIGGMSSSVLDSTYMNLKEEPASK
cfRIP1  513-569  GNTPTIPFSSFPSRDESVKCTIYNSSGIQVGEHNYMEVGGMSSALLD---MNVKEEPAYK
amRIP1  511-567  GNTPTIPFTSFPSRDESVKCAIYNSASIQVGDHNYMEIGGMNSVLPD---MNLKEEPASK
ssRIP1  509-568  GNTPTVPFASLPSRDASPRYILYGNSGVQIGDHNYMELGGASVSVLDSMCPHVKEEPASK
muRIP1  501-556  GSTPTMPYFSGPVADDLIKYTIFNSSGIQIGNHNYMDVG----LNSQPPNNTCKEESTSR
rnRIP1  503-558  GSIPTMPYISLAPPDDSIRCTIYNSSRVQIGNYNYMDLG----PSSQPPTNTCKVESTSR
ggRIP1  504-563  SASQQQKNAADTDTEDSIMYNITNSSGIQIGSHNHMKIEEQNQHISTSSVAKDASYSYYE
hsRIP3  431-490  GMNWSCRTPEPNPVTGRPLVNIYNCSGVQVGDNNYLTMQQTTALPTWGLAPSGKGRGLQH
mmRIP3  431-490  GMNWSSRTPEPNPVTGRPLINLHNCSGVQVGDNNYLTMQQTTALPTGGLAPSGTGRGWQH
cfRIP3  425-483  GTNWPPRAPGPNPIPGSP-ITICDSRAVQVGDYNYLIIQEGTALSTQGQAPWGMGRGWQW
btRIP3  425-484  DTNWPPRGPAPNLVPGPWFPTIFNCQGVQIGNNNRLIIQGGTALSTKGVAPGGVDRGPQC
ssRIP3  429-488  GTNWSPMAPGPNPISGPWSSQLLYNQGVQIGNSNYMVIKGRTASSTRGPVPWGMKKGPQH
rnRIP3  421-477  SNPWYTWNA-PNPMTGLQSIVLNNCSEVQIGQHNCMSVQPRTAFPKKEPAQFGRGRGW--
ecRIP3  422-483  SAHQPPRAPGTDPTPGPPSITVVDCQGVQIGNNNYLYIQGRTTSSTQHPALWGMGWGLTA
muRIP3  421-479  GTPWYPWTP-PNPMTGPPALVFNNCSEVQIGNYNSLVAPPRTTASSSAKYDQAQFGRGRG
                 1.......10........20........30........40........50........60
```

B

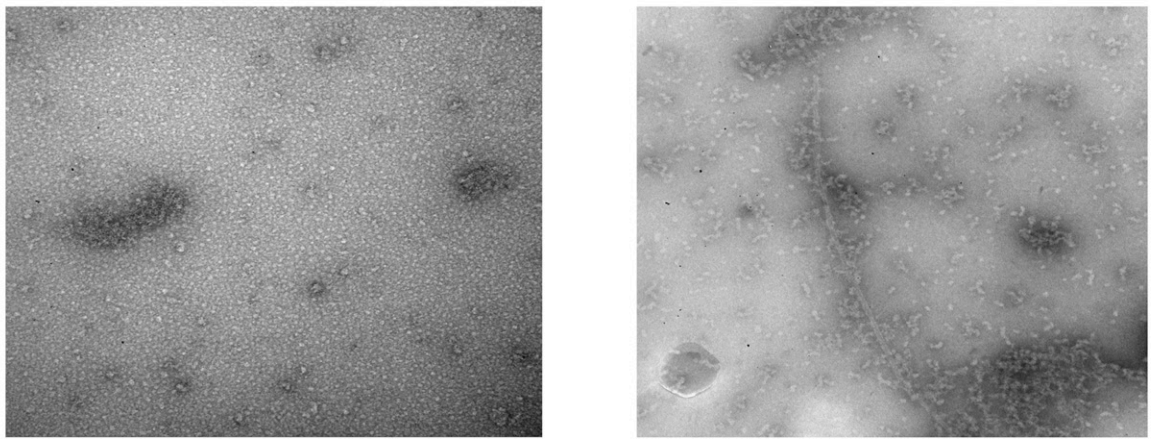

Figure S1. RIP1 and RIP3 Form a Filamentous Complex Using Their RHIMs, Related to Figure 1

(A) Sequence alignment of RIP1 and RIP3 orthologs. Absolutely conserved residues are marked at the top of the alignment. Core residues of the RHIMs are shown above the alignment. hs: *Homo sapiens*; mf: Macaca fascicularis; mm: Macaca mulatta; cj: Callithrix jacchus; ec: Equus caballus; bt: Bos taurus; cf: Canis familiaris; am: Ailuropoda melanoleuca; ss: Sus scrofa; mu: *Mus musculus*; rn: Rattus norvegicus; gg: Gallus gallus. "*" indicates a residue that is absolutely identical among all the orthologs and ":": indicates a residue that is absolutely conserved among all the orthologs. Partially conserved residues are highlighted using color definitions of ClustalX 2.1 (http://ekhidna.biocenter.helsinki.fi/pfam2/clustal_colours). Orange: residue G; Yellow: residue P; Dark cyan: residues H or Y; Cyan: residues W, L, V, I, M, F, A, or C; and Green: residues T, S, N, or Q.

(B) EM images of negatively stained endogenous RIP1/RIP3 complex before (left) and after (right) necrosis stimulation. HT-29 cells were either not stimulated (left) or stimulated (right) with TNF, zVAD-fmk and the IAP antagonist LBW242 to induce programmed necrosis. The RIP1-containing complex was immunoprecipitated with anti-RIP1 antibody, treated with subtilisin (1:50 weight ratio) for 20 min on ice and negatively stained with uranyl acetate.

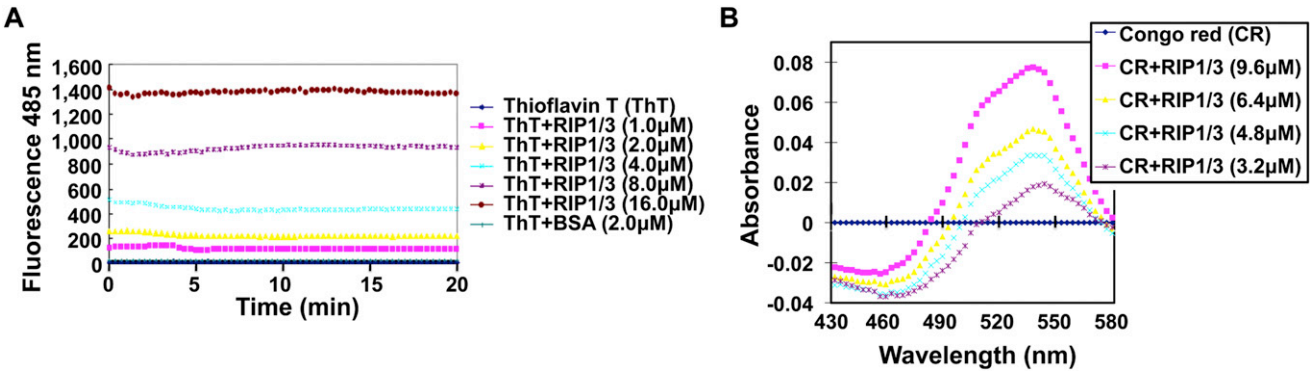

Figure S2. Thioflavin T and Congo Red Binding by RIP1/RIP3-RHIM, Related to Figure 2

(A) Fluorescence emission of ThT at 485 nm in the absence and presence of different concentrations of RIP1/RIP3-RHIM. The excitation wavelength was fixed at 430 nm and the emission was recorded with a band pass of 5 nm.

(B) Absorption difference spectra of CR in the presence of different concentrations of RIP1/RIP3-RHIM.

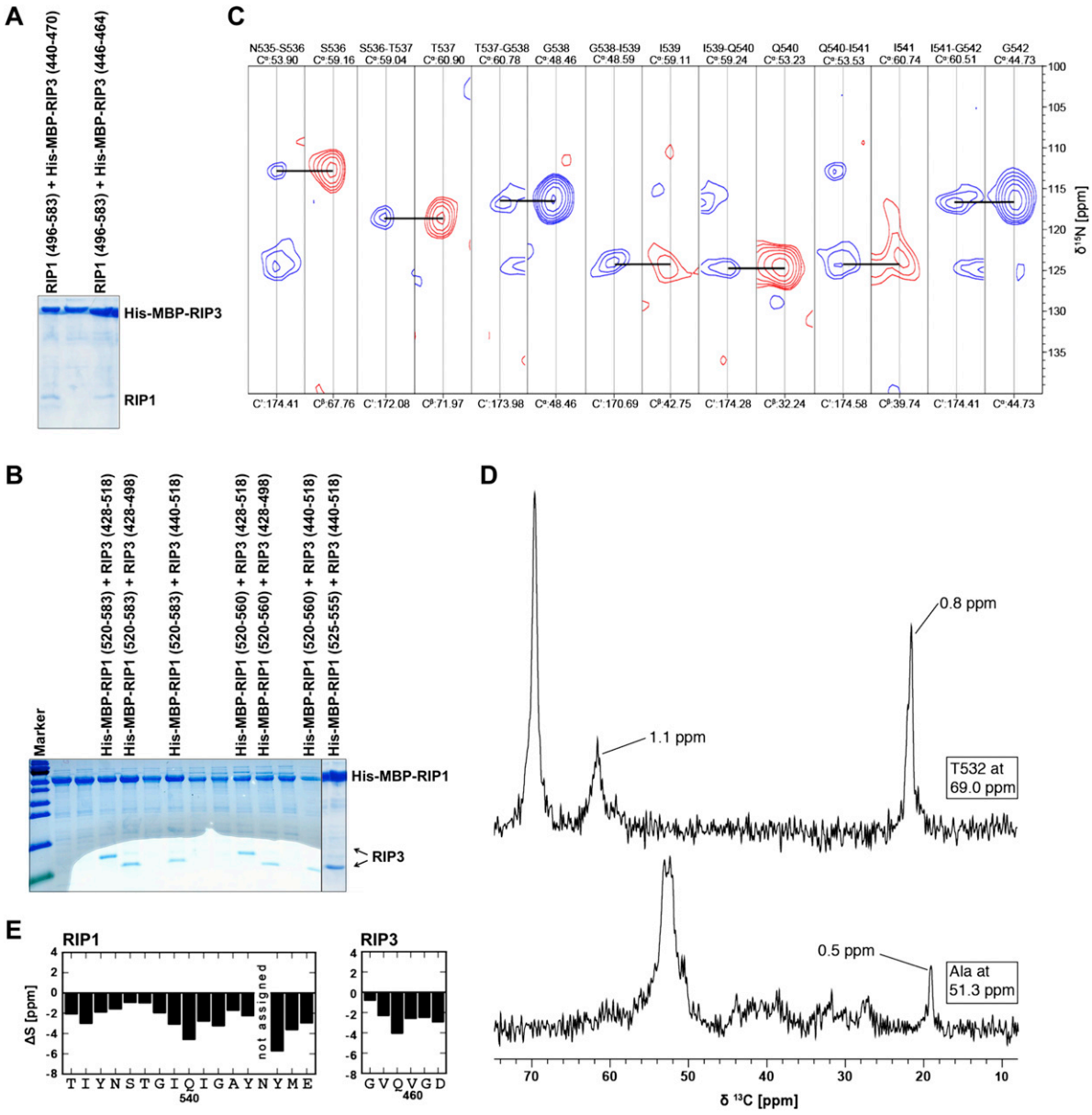

Figure S3. Mapping of the Amyloid Core of the RIP1/RIP3 Complex, Related to Figure 3

(A and B) Mapping the interaction between RIP1 and RIP3 using co-expression and His-tag pull down. Only lanes with positive interactions are labeled. Left panel: RIP1 was tagged with His-MBP. Right panel: RIP3 was tagged with His-MBP.

(C) Strip plots from 3D NCOCA and NCACX experiments illustrating the backbone assignment of RIP1 residues 536-543. Two strips are shown for each residue. The first strip corresponds to the NCOCA spectrum, in which the Cα shift of the strip and the center of the C′ axis (width 3 ppm) are indicated at the top and the bottom of the strip, respectively. The second strip corresponds to the NCACX spectrum. In this case the Cα shift of the strip and the center of the Cβ axis (width 3 ppm) are indicated at the top and the bottom of the strip, respectively. Horizontal lines connect the strips showing $N_i - C'_{i-1} - C^{\alpha}_{i-1}$ and $N_i - C^{\alpha}_i - C^{\beta}_i$ via the common N frequency. The sequential backbone assignment was based on these 3D spectra, the truncated 2D versions (NCoCA and NCaCX), and on $C^{\alpha}_i - C^{\alpha}_{i-1}$ peaks found in 2D DARR spectra.

(D) δ slices of the 2D DARR 900 spectrum shown in Figure 3B. For this figure, the spectrum was processed using no window function in the direct dimension. The δ1 shift of the corresponding slice is given in boxes on the right side. The line width of some nonoverlapping cross-peaks are indicated.

(E) Plot of ΔS, the three-residue average of the secondary chemical shift. ΔS of amino acid i is:

$$\Delta S_i = \frac{1}{3}\left[\left(\delta C^{\alpha}_{i-1} - \delta C^{\beta}_{i-1}\right) + \left(\delta C^{\alpha}_{i} - \delta C^{\beta}_{i}\right) + \left(\delta C^{\alpha}_{i+1} - \delta C^{\beta}_{i+1}\right)\right],$$

where δCx is the difference between the measured and the random coil chemical shift of atom x (also known as secondary chemical shift). A positive value of δCα−δCβ indicates α-helical and a negative value β sheet conformation.

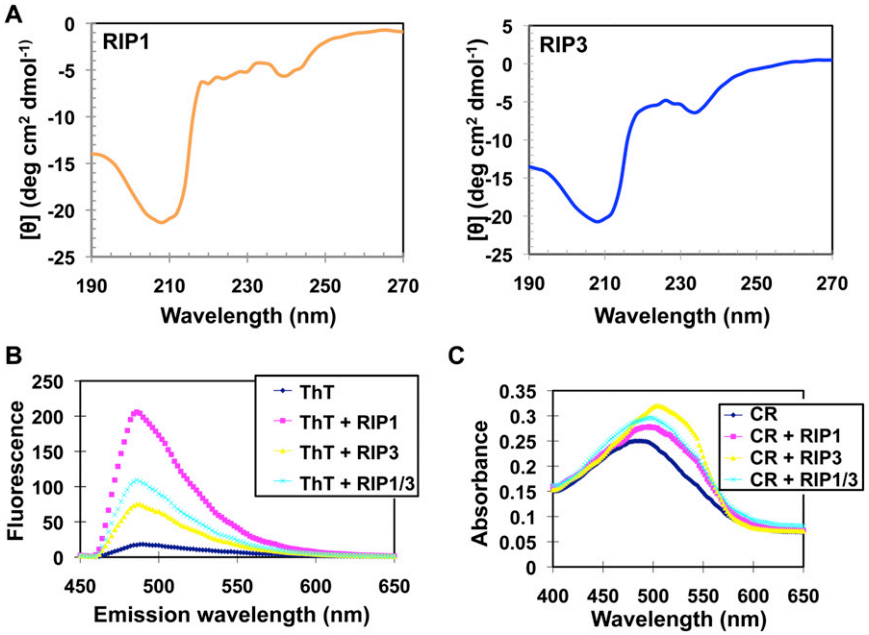

Figure S4. Circular Dichroism, ThT Fluorimetry, and Congo Red Binding of the Individual RIP1 and RIP3 Proteins, Related to Figure 4

(A) CD.

(B) ThT fluorescence.

(C) Congo red absorption.

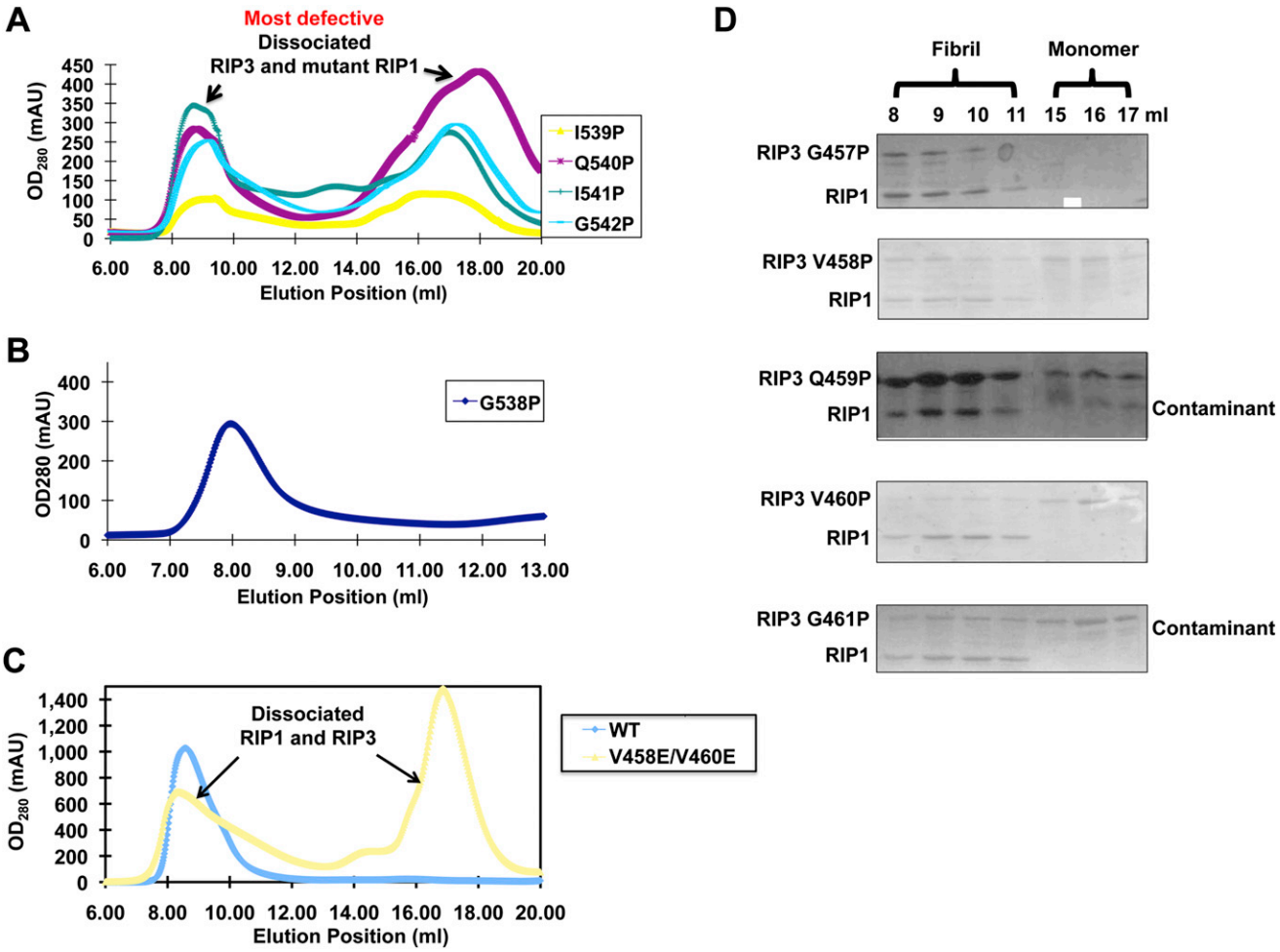

Figure S5. Pro Mutations of RIP1 and RIP3, Related to Figure 5

(A) Superimposed gel filtration profiles of mutant His-RIP1-RHIM co-expressed with WT RIP3-RHIM, showing dissociation of RIP1 and RIP3.

(B) The RIP1-RHIM mutant that did not dissociate from RIP3-RHIM and migrated near the void position.

(C) Gel filtration profile of the His-RIP3-RHIM double mutant (V458E and V460E) co-expressed with RIP1-RHIM, showing the dissociation of RIP1 and mutant RIP3.

(D) SDS-PAGE of RIP3-RHIM mutants co-expressed with WT RIP1-RHIM, showing no dissociation for G457P and partial or near complete dissociation for V458P, Q459P, V460P and G461P.

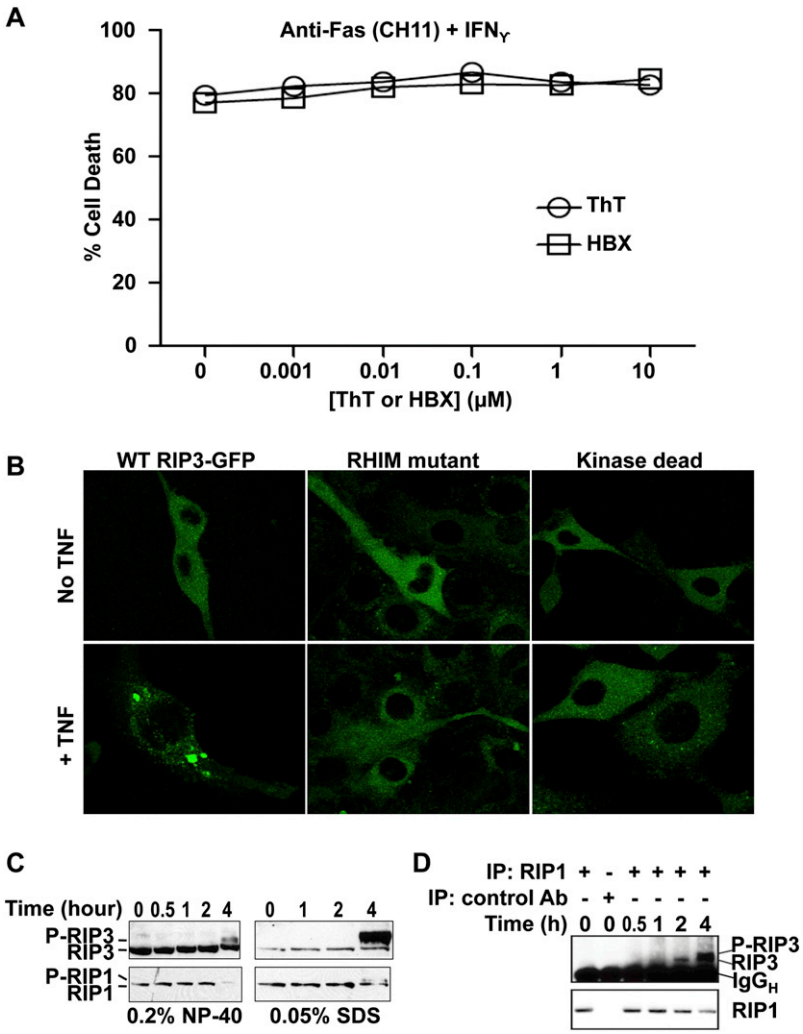

Figure S6. RIP1 and RIP3 Form Amyloidal Clusters In Vivo during Programmed Necrosis, Related to Figure 6

(A) Amyloid binding dyes did not interfere with apoptosis. HT-29 cells were stimulated with anti-Fas antibody and IFNγ in the presence of the indicated amounts of ThT or HBX. Cell death was determined by LDH release assay 36 hr later. Results shown are triplicates of average % cell death ± SEM.

(B) Clustering of RIP3 during necrosis induction requires intact RHIM and kinase domains. RIP3-deficient 3T3 fibroblasts were reconstituted with wild-type, RHIM mutant (AAAA tetra-alanine substitution), or kinase dead RIP3-GFP. Cells were treated with zVAD-fmk alone or TNF and zVAD-fmk for 4 hr. RIP3-GFP was visualized by confocal microscopy.

(C) Phospho-RIP1 (P-RIP1) and phospho-RIP3 (P-RIP3) are preferentially sequestered in NP-40 insoluble compartment. NP-40 soluble total cell lysates were extracted from HT-29 cells treated with TNF, zVAD-fmk and LBW242. The resulting insoluble pellets were extracted with lysis buffer containing 0.05% SDS. Western blot analyses show that P-RIP1 and P-RIP3 were preferentially retained in NP-40 insoluble compartment.

(D) Hyperphosphorylation of RIP3 within the RIP1-associated necrosome. RIP1 complex was isolated from cells treated with TNF, zVAD-fmk, and LBW242 for the indicated times. Recruitment of RIP3 was examined by Western blot. The result shows that RIP3 underwent time-dependent phosphorylation as exhibited by mobility shift of the RIP3 bands between 2 and 4 hr.

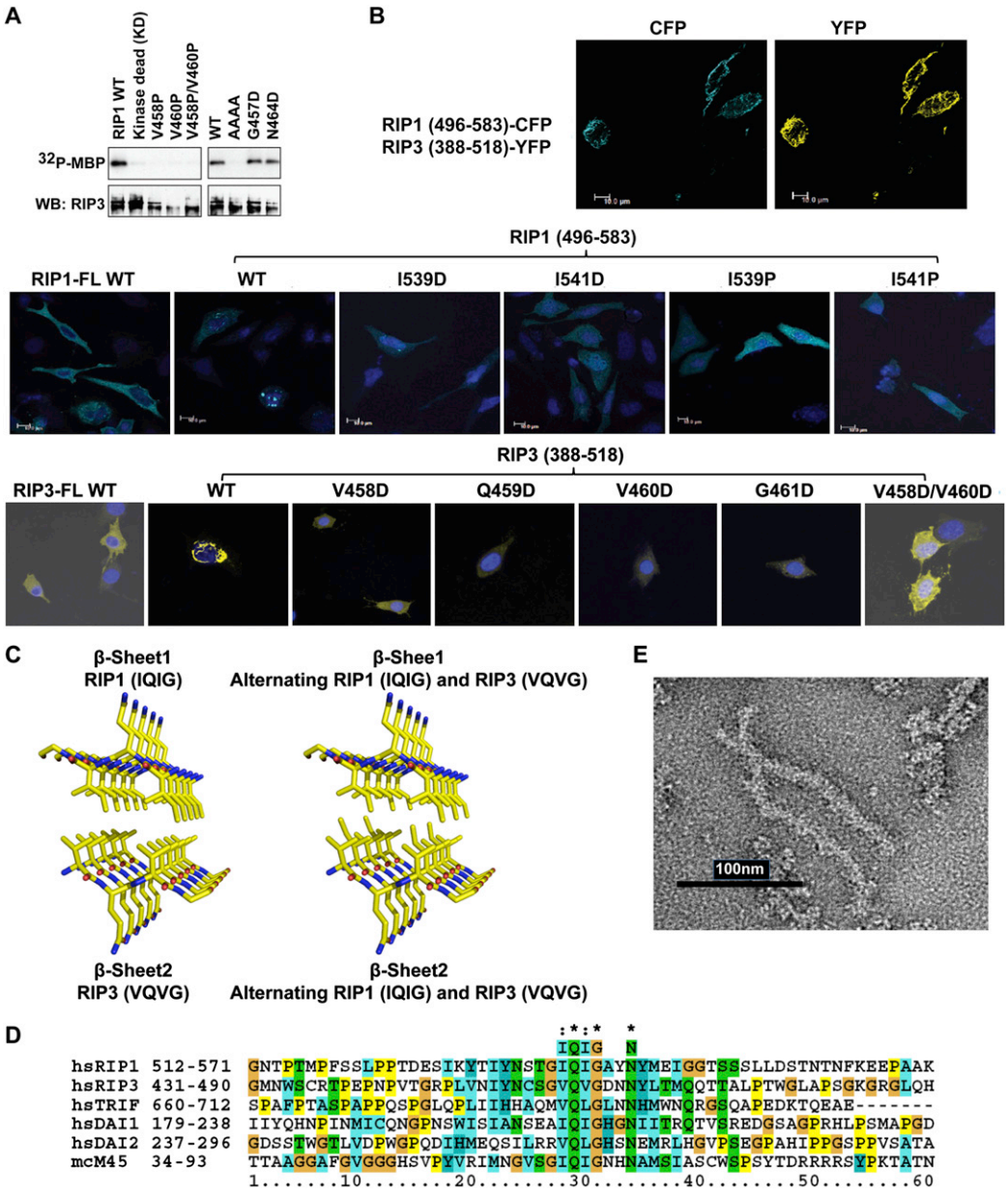

Figure S7. The RIP1/RIP3 Interaction Is Crucial for Kinase Activation, Clustering, and Cell Death, Related to Figure 7

(A) Assessment of kinase activation in RIP1 mutants. The indicated RIP1-GFP constructs were transfected in 293T cells. After immunoprecipitation with anti-GFP antibody, the immune complexes were subjected to in vitro kinase assay using MBP as the substrate. MBP phosphorylation was revealed by autoradiography after transfer of the SDS-PAGE to nitrocellulose membrane. The same membrane was probed for RIP1 on Western blot in the lower panel.

(B) Spontaneous assembly of RIP1-RHIM and RIP3-RHIM fibrils in vivo requires an intact RHIM. The indicated wild-type and mutant RIP1-CFP and/or RIP3-YFP plasmids were expressed in RIP3−/− fibroblasts by transfection. RIP1 and RIP3 were visualized by confocal microscopy. Nuclei were counterstained with DAPI. Note that full length RIP1 and RIP3 exhibit diffuse cytoplasmic staining, while the truncated fragments devoid of the kinase domain and death domain (for RIP1) spontaneously assembled into filamentous clusters. This is consistent with the notion that flanking domains mask the cross β-core of the RHIM and prevent it from aggregation. Mutations within the RHIM core disrupted the spontaneous assembly of these filaments in the truncation RHIM proteins.

(C) Two alternative models of the protofilament structure of the RIP1/RIP3 complex based on the crystal structure of the VQIVYK sequence from tau (PDB code 2ON9).

(D) Sequence alignment of RHIM-containing proteins. Absolutely conserved residues are marked at the top of the alignment. hsRIP1: human RIP1, NP_003795; hsRIP3: human RIP3, NP_006862; hsTRIF: human TRIF, NP_891549; hsDAI1: first RHIM of human DAI, NP_110403; hsDAI2: second RHIM of human DAI, NP_110403; mcM45: mouse cytomegalovirus M45, Q06A28. Partially conserved residues are highlighted using color definitions of ClustalX 2.1 (http://ekhidna.biocenter.helsinki.fi/pfam2/clustal_colours). Orange: residue G; Yellow: residue P; Dark cyan: residues H or Y; Cyan: residues W, L, V, I, M, F, A, or C; and Green: residues T, S, N, or Q.

(E) An EM image of the His-MBP-DAI (residues 150-338)/RIP1 (496-583) complex.